DOI: 10.1111/mice.13012

RESEARCH ARTICLE

COMPUTER-AIDED CIVIL AND INFRASTRUCTURE ENGINEERING WILEY

Analysis of seismically-isolated two-block systems using a multi–rocking-body dynamic model

Giacomo Destro Bisol[1] | **Matthew DeJong**[2] | **Domenico Liberatore**[3] | **Luigi Sorrentino**[1]

[1]Department of Structural and Geotechnical Engineering, Sapienza University of Rome, Rome, Italy

[2]Department of Civil and Environmental Engineering, University of California, Berkeley, California, USA

[3]Department of History, Representation and Restoration of Architecture, Sapienza University of Rome, Rome, Italy

Correspondence
Luigi Sorrentino, Department of Structural and Geotechnical Engineering, Sapienza University of Rome, Via Antonio Gramsci 53, 00197 Rome, Italy.
Email: luigi.sorrentino@uniroma1.it

Abstract

A novel multibody rocking model is developed to investigate the dynamic response of two stacked rigid blocks placed on a linear base isolation device. The model is used to investigate the dynamic response of a realistic statue-pedestal system subject to pulse-like ground motions. The analysis shows that, in general, base isolation increases the safety level of the rocking system. However, for large period pulses or small size blocks, the isolator can amplify the ground motion, resulting in a lower minimum overturning acceleration than for the nonisolated system. Further, the amplification or shock spectrum of a linear mass-dashpot-spring oscillator, was found to be the reciprocal of the minimum nondimensional overturning acceleration of the investigated rocking system. Novel rocking spectra are obtained by normalizing the frequency of the pulse by the frequency of the isolator. The analysis also demonstrates how the dynamic response of the two stacked blocks is equivalent to that of a single-block configuration coincident with the whole system assumed monolithic or the upper block alone, whichever is more slender.

1 | INTRODUCTION

Statues, obelisks, electrical equipment, computer servers, medical equipment, storage systems, and transformers are just a few examples of objects whose behavior can be modeled as rigid rocking objects when subjected to seismic actions (Housner, 1963; Yim et al., 1980; Zhang & Makris, 2001). This study is motivated by the need to protect these nonstructural elements from earthquakes; base isolation systems may be a suitable strategy for this purpose. The problem can be framed into two subjects: (1) rocking response of rigid blocks and (2) base isolation technology to mitigate the response to seismic actions.

Regarding the first subject, the dynamics of rigid blocks is a topic extensively investigated in the last decades, beginning with the pioneering work on a single block performed by Housner (1963), who discovered the well-known scale effect. Housner (1963) pointed out that increasing the size of the block, while keeping the slenderness constant, increases the resistance of the block to overturning due to horizontal ground motion. Yim et al. (1980) investigated the dynamic behavior of a rigid block, highlighting the high sensitivity of this type of system to geometry and ground motion. Further, the response of a rigid block subjected to pulse-like ground motion was investigated using rocking spectra (Zhang & Makris, 2001); this type of depiction proved to be particularly effective, allowing an immediate understanding of the response for different geometries and different pulses. Dimitrakopoulos and DeJong (2012) then developed the analytical formulation

of the rocking spectra for sine pulses. Moreover, rigid block modeling has recently gained attention for the assessment of the seismic vulnerability of nonstructural elements (Dar et al., 2016; Fragiadakis & Diamantopoulos, 2020; Vlachakis et al., 2021).

Base isolation technology for earthquake protection has also been extensively investigated in recent decades. Numerous studies in the field of response control (Fantuzzi et al., 2022; Noureldin et al., 2021) and seismic isolation (Housner et al., 1996; Naeim & Kelly, 1999) have been conducted worldwide (Lin et al., 2010; Saleh & Adeli, 1998), and significant advances in the innovation of these technologies have been made (El-Khoury & Adeli, 2013; Higashino & Okamoto, 2006). Structural control devices can be classified into three categories: "passive control" (Froli et al., 2019; Narasimhan et al., 2006; Salvatore et al., 2021), "semi active control" (Gutierrez Soto & Adeli, 2019; Naderpoor & Taghikhany, 2022; Shi et al., 2021), and "active and hybrid control" (Bitaraf et al., 2012; Kim & Adeli, 2005a) systems. Recently, in the field of seismic protection, important advancements have been made (Gutierrez Soto & Adeli, 2018; Javidan & Kim, 2022; Xu et al., 2021), and researchers focused their attention on different vibration control technologies such as tuned mass dampers (Kayabekir et al., 2022; Kim & Adeli, 2005b). Base isolation devices have found their primary application in vibration control of buildings (Gutierrez Soto & Adeli, 2017; Kim & Adeli, 2005c; Li & Adeli, 2018) and bridges (Ghaedi et al., 2017; Kim & Adeli, 2005b). Here, the interaction between rocking systems and isolators is thoroughly investigated. Only passive control systems, which mitigate seismic response without the need of electric energy, are considered for this purpose.

Seismic isolation technology used in the protection of rocking rigid blocks (Di Egidio & Contento, 2009; Di Egidio, Contento, De Leo, et al., 2020a; Di Egidio, Contento, Olivieri, et al., 2020b) received attention, mainly to preserve valuable slender art objects (Baggio et al., 2018; Berto et al., 2013; Fragiadakis & Diamantopoulos, 2020). These studies generally confirmed the efficiency of the seismic isolation technology (Baggio et al., 2015; Caliò & Marletta, 2003; Roussis et al., 2008). According to Vassiliou and Makris (2012), base isolation may not improve the performance of large free-standing structures. Recently, the emphasis has shifted to the investigation of novel constitutive laws for the isolation system (Pellecchia et al., 2020, 2022) or innovative protection technologies (Amarante dos Santos & Fraternali, 2022; De Canio, 2012; Venanzi et al., 2020).

There are also cases where one block is placed on top of another, and the single rigid body model is unable to adequately define the dynamic response. Stacked servers, medical shelves, a piece of machinery on a base and ancient columns are real-life examples. Particularly relevant is the case of two blocks one on top of the other, such as an art object placed on a pedestal (Figure 1). The response of this type of system was explored by Psycharis (1990), Spanos et al. (2001), Chatzis et al. (2018), and Diamantopoulos et al. (2022). The authors draw the conclusion that the formulation of this extremely nonlinear analytical model is challenging, due in part to highly nonlinear equations of motion, impacts, and continually changing contacts (Bao & Konstantinidis, 2020). Further studies on the two-block assemblies were conducted in the field of out-of-plane mechanisms for masonry structures (Lourenço et al., 2011), with the goal of investigating a two-block vertically spanning wall mechanism (DeJong & Dimitrakopoulos, 2014; Prajapati et al., 2022; Sorrentino et al., 2008).

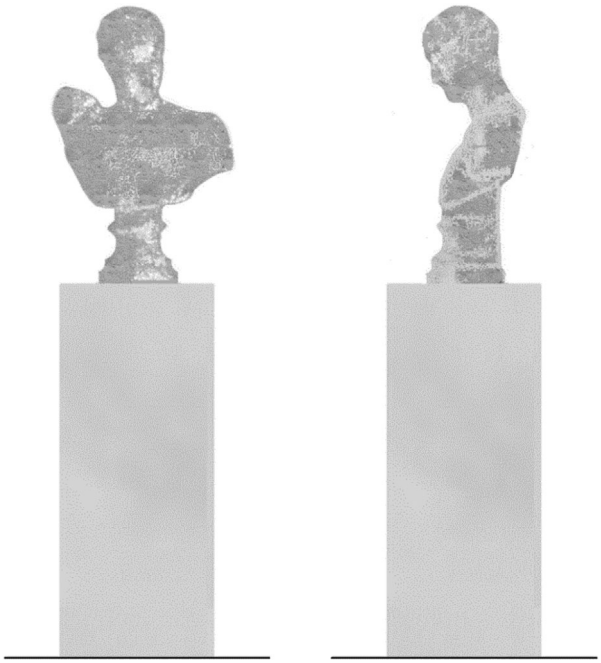

FIGURE 1 Example of a real-life two stacked rigid block system: A Roman bust placed on a pedestal.

Further, a variety of experimental tests have been conducted to investigate the response of rocking objects, such as medical shelves (Kuo et al., 2011), art objects (Huang et al., 2022), display cases (Prota et al., 2022), and hospital cabinets (Di Sarno et al., 2019). Fragiadakis et al. (2020) carried out a large experimental campaign on several bust-pedestal systems placed on a base isolation device. Despite the above-mentioned test, an analytical model capable of capturing the response of a seismically isolated two stacked rigid blocks system (Figure 2) has not been developed to date.

In this paper, a new computational model is developed to analyze the response of two stacked rocking blocks resting on flexible elements (such as a base isolation device). There are similarities between the proposed model

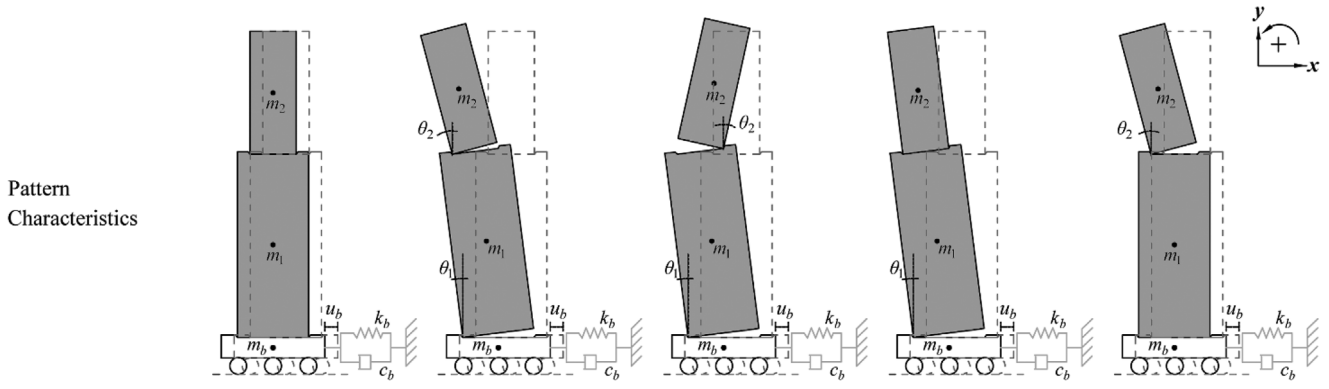

Label	0	1a	2a	3a	4a
Lagrangian Parameter (DOF)	u_b	$u_b\,;\theta_1\,;\theta_2$	$u_b\,;\theta_1\,;\theta_2$	$u_b\,;\theta_1$	$u_b\,;\theta_2$
Assumptions	$\theta_1=\theta_2=0$	$\theta_2>\theta_1>0$	$\theta_1>0\,;\theta_2<\theta_1$	$\theta_1=\theta_2>0$	$\theta_1=0\,;\theta_2>0$

FIGURE 2 Motion patterns of the seismically isolated two stacked rigid blocks system (patterns 1b, 2b, 3b, 4b are reversed with respect to 1a, 2a, 3a, 4a, respectively).

and multibody dynamics (MBD), which is the topic of computer modeling and analysis of constrained bodies subject to large displacements and rotations (Shabana, 1997). This paper illustrates in detail a multi–rocking-body dynamic (MRBD) model capable of describing the dynamics of a three degree-of-freedom (DOF) system; the model is then used to examine the response of the two stacked blocks placed on an isolator when subject to sine-pulse ground motion.

The real-life objects at the base of the model in Figure 2 are 3D in nature. However, the investigation of the 3D dynamic response, including base isolation, would typically be investigated numerically, for example by means of the discrete element method (Malomo et al., 2021) or the finite-discrete element method (AlShawa et al., 2017), because deriving the analytical equations of motion for a range of 3D geometries is impractical. Nonetheless, analytical equations provide a powerful tool to identify general trends of the response for a large range of the values of the system parameters, and therefore can guide the design of base isolation intervention. Therefore, analytical equations are derived in the following for a representative 2D system.

The first part of the study focuses on the description of the kinematic quantities, energies, and nonconservative forces, followed by the derivation of the equations of motion (via a Lagrangian approach) for each possible rocking mode. Following the description of all possible transitions between rocking modes (or patterns), the solution algorithm is presented as well using pseudo-code.

In the second part of the paper, the effect of base isolation on a realistic statue-pedestal system is investigated, and significant results for both the two stacked blocks system and the single rocking block have emerged. The response of this type of system to pulse-like ground motion can be expressed using rocking spectra, which are typically built by assuming the ratio between the pulse period and period of the isolator is constant (Vassiliou & Makris, 2012). In this study, rocking spectra derived by assuming the period of the base isolation as constant are compared to the previous typology, and the benefits and drawbacks of the two types of spectra are discussed. Interesting results are also obtained using shock spectra for linear mass-dashpot-spring (LMDS) oscillators subjected to pulse-like ground motion; a direct relation between minimum overturning nondimensional acceleration of rigid blocks and maximum amplification of the LMDS oscillator is discovered. Moreover, minimum acceleration overturning spectra are derived using a different normalization criterion for the pulse frequency, which has previously been normalized with respect to the frequency parameter of the rigid block (Pellecchia et al., 2022; Vassiliou & Makris, 2012; Zhang & Makris, 2001). The use of this novel criterion allows the response to be expressed in terms of a rocking spectrum independent of the isolator period, allowing other parameters to be investigated. The previous observations are generally applicable to both single-block and two stacked block models, hence additional analysis on the two-block assembly was performed. Previous research on this topic has focused on the dynamics and energy dissipation of the system (Chatzis et al., 2018; Psycharis, 1990; Spanos et al., 2001); here, dynamic equivalence with a single rocking block is found as long as a specific configuration is used. Finally, the paper concludes with practical observations

for designing base isolation devices for rocking objects and enhancing the safety level of the system.

2 | EQUATIONS OF MOTION

The MRBD system of this study is an assembly of two stacked rigid blocks, both free to rock, placed on a seismic isolation device. Friction is assumed to be sufficiently large to prevent sliding between the two blocks and between the lower block and the isolator. Sliding is usually beneficial, provided that the block does not impact other objects or walls, and provided that the upper block does not fall from the lower one (Kounadis, 2018). Hence, an isolator design based on the no-sliding assumption is generally conservative. Here, the behavior of the isolator is assumed to be linear, hence the base isolation system adds one DOF and it can be described by the mass m_b, the stiffness k_b, and the viscous damping c_b (all symbols presented herein are listed in Table D1 of Appendix D). The lower and upper blocks have thicknesses $2b_1$ and $2b_2$, respectively, while the height of the lower block is $2h_1$ and that of the upper block is $2h_2$. Further, the lower block has mass m_1, while the upper has mass m_2. If the joint between the blocks is closed and the two blocks move together, the following parameters can be defined: (1) the total mass of the blocks, $m = m_1 + m_2$; (2) the height, h, of the combined center of mass.

The system is characterized by five modes or patterns (Figure 2), and the equation of motion must be formulated for each one of them. Due to the several variables and to the different motion patterns, variational methods are adequate for deriving the equations of motion of the MRBD model, avoiding the calculation of internal forces (Fabien, 2008; Humar, 1990; Meirovitch, 1970). The system studied here has three DOFs, the rotations θ_1 and θ_2 of the lower and of the upper block, respectively, and the horizontal displacement of the isolator u_b.

The analytical equation of motion for each pattern is obtained using a Lagrangian approach, deriving with respect to the time the kinetic energy, the potential energy, and the dissipation function, as well as calculating the nonconservative forces.

As shown in Figure 2, each pattern is characterized by a specific number of Lagrangian parameters, and the same number of equations of motion, one for each generalized coordinate.

2.1 | Kinematic analysis

Once the generalized coordinates are defined, it is convenient to define displacement, position, and velocity vectors to describe the motion of the center of mass of each body. During the motion, for example, in pattern 2a (Figure 2), the system can be seen as two constrained rigid bodies rotating around an LMDS oscillator (Figure 3), where the hinges represent the contact points of the rigid blocks.

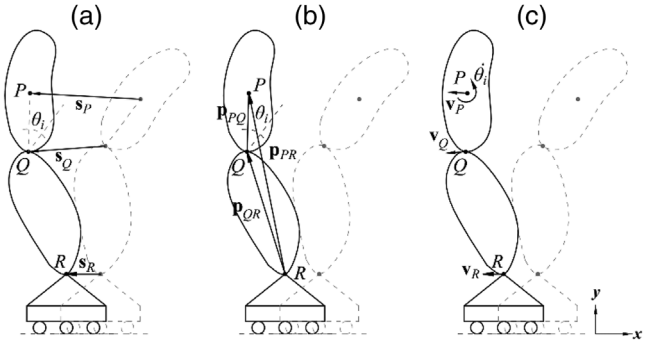

FIGURE 3 Kinematic vectors calculation: (a) displacement; (b) position; (c) velocity.

In this case, the displacement of the generic point P, belonging to the upper body rotating with angle θ_i about Q, can be described, with reference to the global axes x-y, by means of the displacement vector $\mathbf{s}_P$:

$$\mathbf{s}_P = \mathbf{s}_Q + \mathbf{S}_{T_i} \cdot \mathbf{d}_{P,Q} = \begin{Bmatrix} s_{Q,x} \\ s_{Q,y} \\ 0 \end{Bmatrix} + \begin{pmatrix} \cos\theta_i - 1 & -\sin\theta_i & 0 \\ \sin\theta_i & \cos\theta_i - 1 & 0 \\ 0 & 0 & 0 \end{pmatrix} \cdot \begin{Bmatrix} x_P - x_Q \\ y_P - y_Q \\ 0 \end{Bmatrix} \tag{1}$$

where $\mathbf{s}_Q = \mathbf{s}_R + \mathbf{S}_{T_i} \cdot \mathbf{d}_{Q,R}$ is the known displacement vector of point Q, $\mathbf{s}_R$ is the known displacement vector of point R belonging to the LMDS oscillator, $\mathbf{S}_{T_i}$ is the displacement vector transformation matrix of the i-th block, $\mathbf{d}_{P,Q}$ ($\mathbf{d}_{Q,R}$) is the vector that contains the coordinates, x and y, of the generic point P (Q) with respect to the center of rotation Q (R) in the global reference system x-y.

Similarly, it is possible to define a position vector $\mathbf{p}_{P,R}$, used to evaluate the velocity of any point and the angular momentum of a rigid body:

$$\mathbf{p}_{P,R} = \mathbf{p}_{Q,R} + \mathbf{P}_{T_i} \cdot \mathbf{d}_{P,Q} = \begin{Bmatrix} p_{Q,R,x} \\ p_{Q,R,y} \\ 0 \end{Bmatrix} + \begin{pmatrix} \cos\theta_i & -\sin\theta_i & 0 \\ \sin\theta_i & \cos\theta_i & 0 \\ 0 & 0 & 0 \end{pmatrix} \cdot \begin{Bmatrix} x_P - x_Q \\ y_P - y_Q \\ 0 \end{Bmatrix} \tag{2}$$

where $\mathbf{p}_{Q,R}$ is the known position vector of the point Q, $\mathbf{P}_{T_i}$ is the transformation matrix for the position vector, which allows the expression of the position vector of the generic point as a function of the main reference system.

Furthermore, to compute the kinetic energy, the velocity of the centers of mass must be calculated for all bodies. In the case of the generic point P, which belongs to a rigid body that rotates with angular velocity $\dot{\theta}_i$ about the point Q, the generic velocity vector is:

$$\mathbf{v}_P = \mathbf{v}_R + \mathbf{v}_Q + \dot{\boldsymbol{\theta}}_i \times \mathbf{p}_{P,Q} \tag{3}$$

where $\mathbf{v}_R$ is the known velocity vector of the point R, $\mathbf{v}_Q = \dot{\boldsymbol{\theta}}_i \times \mathbf{p}_{Q,R}$ is the relative velocity vector of point Q, $\dot{\boldsymbol{\theta}}_i$ is the angular velocity vector, and $\times$ is the vector product operator.

These vectors can be obtained knowing only the Lagrangian parameters and the coordinates of the points, allowing a certain convenience in computing the equation of motion for MRBD systems. Once these vectors are known, the kinetic and potential energy as well as the nonconservative forces, used to assemble the Lagrangian equations of motion, can be easily derived for any kind of MRBD system.

2.2 | Lagrange's equation

The kinetic energy T can be derived as:

$$T = \frac{1}{2} m_b |\mathbf{v}_{Gb}|^2 + \sum_{i=1}^{2} \left[\frac{1}{2} \left(m_i |\mathbf{v}_{Gi}|^2 + I_{Gi} \dot{\theta}_i^2 \right) \right] \tag{4}$$

where $|\mathbf{v}_{Gi}|$ is the magnitude of the velocity vector of the i-th center of mass, I_{Gi} is the mass moment of inertia of the i-th block with respect to its centroid G, m_i is the mass of the i-th block, the b subscript is related to the base isolator, and the dot superscript indicates derivative with respect to time.

The potential energy, V, and the dissipation function, D, can be obtained as:

$$V = \frac{1}{2} k_b u_b^2 + \sum_{i=1}^{2} g\, m_i\, p_{Gi,y}; D = \frac{1}{2} c_b \dot{u}_b^2 \tag{5}$$

where $p_{Gi,y}$ is the vertical component of the position vector of the center of mass of the i-th body.

The last step to build the equations of motion is the applied effort analysis, which provides the nonconservative forces (one for each generalized coordinate) using the virtual work δW_{nc}:

$$\delta W_{nc} = -m_b\, \ddot{x}_g\, \delta u_b - \ddot{x}_g \sum_{i=1}^{2} m_i\, \delta s_{G_i,x} - \ddot{y}_g \sum_{i=1}^{2} m_i \delta s_{G_i,y} \tag{6}$$

where $\delta s_{G_i,x}$ and $\delta s_{G_i,y}$ are, respectively, the horizontal and vertical components of the virtual displacement vector of the i-th center of mass, $\ddot{x}_g$ and $\ddot{y}_g$ are, respectively, the horizontal and vertical components of the seismic ground acceleration. Writing δu_b, $\delta s_{G_i,x}$, and $\delta s_{G_i,y}$ as functions of the virtual generalized coordinates provides the generalized forces.

The approach previously explained is used for the patterns characterized by three DOFs (patterns 1 and 2). In the case of pattern 3, it is necessary to assume the rotations of the upper and lower blocks equal. Regarding pattern 4, it is sufficient to assume the rotation of the lower block equal to zero. For pattern 0, both the rotations θ_1 and θ_2 must be assumed equal to zero. A practical example can be found in Appendix A.

3 | PATTERN CHANGE

The two-block system can change pattern during motion due to impacts or acceleration thresholds exceeded (Prajapati et al., 2022; Psycharis, 1990; Spanos et al., 2001). In this case, where the blocks are placed on a seismic isolation device, three major differences in the formulation of pattern changes are found in comparison to the nonisolated system.

The first concerns the beginning of motion: differently from the nonisolated system, the motion is not triggered by a threshold acceleration, and the base isolation device is activated for any amplitude of the ground motion. In the isolated case, the system begins its motion in pattern 0, then for each step of the integration, a check of rocking motion initiation is performed.

The second difference regards the pattern change due to acceleration thresholds exceeded. Although the procedure is the same as the one proposed in Spanos et al. (2001) and Prajapati et al. (2022), where internal and external moments are set equal, here the external accelerations of the isolation device must be included in the computation of the external moments.

The third difference is in the calculation of the coefficient of restitution after collision occurs: In the isolated system, the lower block impacts with a device of finite mass (the isolator) instead of a rigid foundation.

3.1 | Pattern change due to acceleration thresholds exceeded

If the ground motion is large enough, rocking will initiate and the system will change its pattern. The problem is generally solved by setting the external moment equal to the internal moment in order to find a threshold acceleration to detect the change (Spanos et al., 2001). In the case at hand, the procedure for evaluating this threshold acceleration is similar to that in Prajapati et al. (2022), but has been appropriately modified to account for the effect of the base isolation system.

External moments are generated by inertia forces originating from the ground (and isolator) motion, which are defined in the external acceleration vector $\mathbf{a}_E$:

$$\mathbf{a}_E = \left\{-\ddot{x}_g - \ddot{u}_b, -\ddot{y}_g - g, 0\right\}^T \tag{7}$$

Then, the external moment vector $\mathbf{M}_E$ can be calculated as follows:

$$\mathbf{M}_E = \sum_{i=1}^{2} m_i \left(\mathbf{p}_{G_i}^{+} \times \mathbf{a}_E\right) \tag{8}$$

where $\mathbf{p}_{G_i}^{+}$ is the position vector of the i-th center of mass with respect to the center of rotation associated with the pattern to which the system could change if the threshold acceleration is reached. The patterns before and after the change are denoted by $^-$ and $^+$, respectively.

To compute the internal moments, the normal and tangential accelerations of the masses must be calculated in each instant prior the possible pattern change; these accelerations are computed with respect to the pattern before the possible change as follows:

$$\mathbf{a}_{G_i,n} = -\mathbf{p}_{G_i}^{-}\dot{\theta}_i^2;\ \mathbf{a}_{G_i,t} = \mathbf{p}_{G_i}^{-} \times \left(-\ddot{\boldsymbol{\theta}}_i\right) \tag{9}$$

where $\mathbf{a}_{G_i,n}$ and $\mathbf{a}_{G_i,t}$ are, respectively, the normal and the tangential acceleration vector of the i-th center of mass, $\ddot{\boldsymbol{\theta}}_i$ is the angular acceleration vector, and $\mathbf{p}_{G_i}^{-}$ is the position vector of the i-th center of mass with respect to the pattern before the possible change.

The internal moment vector $\mathbf{M}_I$ can then be calculated with respect to the pattern in which the system could change its motion as follows:

$$\mathbf{M}_I = I_{G_i}\,\ddot{\boldsymbol{\theta}}_i + m_2\left(\mathbf{p}_{G_i}^{+} \times \mathbf{a}_{G_i,n} + \mathbf{p}_{G_i}^{+} \times \mathbf{a}_{G_i,t}\right) \tag{10}$$

Finally, by setting internal and external moments to be equal, the minimum acceleration $\ddot{x}_{j,k}$ for which the system can transition from pattern j to pattern k can be determined (Equation 11).

$$M_{I,z} = M_{E,z} \rightarrow \ddot{x}_{j,k} \tag{11}$$

where $M_{I,z}$ and $M_{E,z}$ are, respectively, the rotational component of the internal and external moment vectors.

The principal difference between the isolated and nonisolated cases is the beginning of rocking motion. The uplift acceleration, which causes rocking motion, can be viewed as a further pattern change caused by an external acceleration and calculated using the previous equations. In Appendix B, more details on pattern changes without impacts can be found.

3.2 | Pattern change due to impacts

An impact can occur between the upper and lower blocks (middle impact) or between the lower block and the isolator (lower impact); if this happens, the system starts to move in another pattern with consequent energy loss. Here, impacts are assumed to be instantaneous, moreover only one impact can occur at a given instant. Further, if the impact is assumed to be inelastic (no bouncing), the rotation continues smoothly from one corner to the other, and the angular momentum about is conserved as customary in rocking dynamics (Housner, 1963) and reasonably confirmed by experiments (Sorrentino et al., 2011).

As previously described in Spanos et al. (2001) and Prajapati et al. (2022), the analytical coefficient of restitution must be estimated for each type of pattern change due to impacts. The distinction between the nonisolated case and that where the system is placed on an isolator is in the calculation of the postimpact velocities. When an impact occurs, the base isolation also undergoes a change in velocity (Vassiliou & Makris, 2012). For the model of two stacked rigid blocks placed on a finite mass isolator, the new velocities after impact must be evaluated for all three Lagrangian parameters. The postimpact velocities are computed by solving a system of three equations (Equation 12), obtained using conservation of momentum principles, and more specifically: (1) conservation of angular momentum of the entire system $\mathbf{H}_{sys}$, (2) conservation of angular momentum of the top block only $\mathbf{H}_{top}$, and (3) conservation of linear momentum in the horizontal direction $g_{sys,x}$. The momentums must be calculated with respect to the pattern before (−) and after (+) the impact.

$$\begin{cases} \mathbf{H}_{sys}^{-} = \mathbf{H}_{sys}^{+} \\ \mathbf{H}_{top}^{-} = \mathbf{H}_{top}^{+} \\ g_{sys,x}^{-} = g_{sys,x}^{+} \end{cases} \tag{12}$$

The angular momentum of the entire system is obtained as follows:

$$\mathbf{H}_{sys} = \sum_{i=1}^{2} I_{Gi}\dot{\theta}_i + \sum_{i=1}^{2} \mathbf{p}_{G_i} \times m_i \mathbf{v}_{G_i} \tag{13}$$

The angular momentum of the upper body alone can be derived using Equation (14).

$$\mathbf{H}_{top} = I_{G_2}\,\dot{\theta}_2 + \mathbf{p}_{G_2} \times m_2 \mathbf{v}_{G_2} \tag{14}$$

The linear momentum in the horizontal direction can be obtained as follows:

$$g_{sys,x} = m_b v_{G_b,x} + \sum_{i=1}^{2} m_i v_{G_i,x} \tag{15}$$

Further, after each type of impact, whether lower or middle, the system can transit to an a priori assumed pattern, after which angular velocities are controlled to assess kinematic admissibility. If it is not satisfied, the system will switch to an alternative pattern (Prajapati et al., 2022). Further information about transitions due to impacts can be found in Appendix C, while the postimpact velocities for every possible pattern change are presented in Destro Bisol et al. (2023).

MRBD Algorithm: Basc Isolation of Two Stacked Rocking Blocks

```
1. procedure
2.     input ← [b1, b2, h1, h2, mb, kb, cb, ẍg, ÿg] \\ input data
3.     start
4.       while system is in motion  do
5.         switch
6.           case pattern \\ repeat for pattern 0,1,2,3,4.
7.             start with pattern 0
8.             integrate differential equation for specific pattern
9.             \\event function
10.              if pattern change w/o impact detected
11.                 update pattern case \\ Table B. 1
12.              elseif impact detected \\ θ1= 0 or  θ1= θ2
13.                 calculate velocities after impact \\θ̇1+, θ̇2+, u̇b+
14.                 if kinematic assumption check true \\ Table C. 1
15.                    update pattern case
16.                 else
17.                    calculate velocities after impact \\ θ̇1+, θ̇2+, u̇b+
18.                    update pattern case
19.                 end if
20.              elseif overturning detected \\ θ1= π/2 or θ2 = π/2
21.                 end loop
22.              elseif stop rocking motion detected
23.                 update pattern case to pattern 0
24.              elseif end of ground motion and small total energy
25.                 end loop
26.              end if
27.        end switch
28.      end while
29. end procedure
```

FIGURE 4 MRBD system solution algorithm.

4 | SOFTWARE DEFINITION

Once the equations of motion are obtained and the pattern changes are defined for each possible transition, the response of the system to ground motion was simulated. The solution algorithm, implemented in MATLAB (2018), is briefly summarized in Figure 4 using a pseudocode scheme

The analysis can start once the input data, that is, the geometric and mechanical properties and ground motion excitation, are defined. The first stage is the integration of the equation of motion for pattern 0; the integration continues until an event occurs. From pattern 0, two possible events can occur: (a) rocking motion starts without impact; (b) the system stops, that is, comes to rest. If the threshold acceleration of Equation (11) is overcome, rocking motion starts (event a) and the pattern in which the system is moving must be updated, a new case must be assumed for the switch function (Figure 4, line 6) and the integration of the specific equation of motion is restarted.

Once the system is moving in a rocking pattern (either 1, 2, 3, or 4), the following events can occur: (a) pattern change without impact (Figure 4, line 10); (b) pattern change with impact (Figure 4, line 12); (c) overturning (Figure 4, line 20). If event (a) occurs, the integration continues with the new pattern, all these possible transitions are defined in Table B1. If event (b) takes place, impact occurs, and the postimpact velocities must be calculated (Figure 4, line 13) in relation to the primary pattern (Table C1) in which the system can move; then the kinematic check must be performed. If the kinematic check is satisfied, the integration can proceed in the new pattern with the newly calculated postimpact velocities. If it is not satisfied, the postimpact velocities must be calculated (Figure 4, line 17) with respect to the secondary pattern (Table C1) in which the system can switch, and the integration continues with the new pattern. If event (c) occurs, the system (or part of it) has overturned: In this case, the analysis stops, and the while cycle is interrupted.

5 | RESPONSE TO PULSE-TYPE GROUND MOTION

The developed computational software can be employed for any type of ground excitation, with earthquake ground motion being the most important in terms of potential damage to the blocks investigated here. However, record selection can be performed only with a specific system at a specific location in mind and usually would involve

modeling the building that houses the system (D'Angela et al., 2021, 2022; Giouvanidis & Dimitrakopoulos, 2018). Therefore, in order to get a general understanding of the dynamic response of the MRBD model, as well as to derive general trends in its behavior, a pulse-like ground motion is considered. Conveniently, the response to this input can be expressed in dimensionless plots using rocking spectra (Zhang & Makris, 2001). These spectra are nondimensional, allowing exploration of a range of pulses with different amplitude and period, or a range of systems with different slenderness and size. For this purpose, the slenderness α (α_2), the size parameter R (R_2), and the frequency parameter p (p_2) are introduced for two cases: (a) two-block assembly considered as monolithic, that is, interface between upper and lower block is closed (Equation 16); (b) upper block alone (Equation 17).

$$\alpha = \tan^{-1}\left(\frac{b_1}{h}\right); R = \sqrt{b_1^2 + h^2}; p \approx \sqrt{3g/4R} \quad (16)$$

$$\alpha_2 = \tan^{-1}\left(\frac{b_2}{h_2}\right); R_2 = \sqrt{b_2^2 + h_2^2}; p_2 = \sqrt{3g/4R_2} \quad (17)$$

The previous equations are derived under the assumptions that both blocks are homogeneous and share the same density. The base isolation device can be described using the period T_b, the mass ratio γ_b, and the damping ratio ξ_b as described in Equation (18). Additionally, the pulse amplitude is denoted as a_p, the pulse circular frequency is named ω_p, and the pulse period is denoted as T_p.

$$T_b = 2\pi\sqrt{M/k_b}; \gamma_b = \frac{m}{M}; \xi_b = \frac{c_b}{2\omega_b M} \quad (18)$$

where ω_b is circular frequency of the isolator, and $M = m + m_b$ is the total mass.

The behavior of the system and its sensitivity to the different parameters are described starting from an application where the real-life system in Figure 1 is approximated using the model in Figure 5a, with appropriate parameters. The lower block of the investigated system has a height of $2h_1 = 1.0$ m, and a thickness of $2b_1 = 0.4$ m, whereas the upper block has a height of $2h_1 = 0.75$ m and a thickness of $2b_2 = 0.22$ m; it is assumed that the two blocks have the same density. The mechanical properties of the base isolation for the investigated system can be summarized as follows: (a) period $T_b = 2.0$ s; (b) mass ratio $\gamma_b = 0.9$; (c) damping ratio $\xi_b = 0.05$. This scenario is referred to as the "reference system" in this paper; variations to this reference system will be considered later in the paper.

The response of the reference system to a sine-pulse ground motion (Figure 5b) is shown in terms of displacement of the base isolator (Figure 5c), of rotation of each of the two blocks (Figure 5d), and in terms of pattern (Figure 5e). The system begins to move in pattern 0 at the onset of the ground motion, then the system starts to rock in pattern 3 due to a large acceleration. As the acceleration increases, another pattern change without impact occurs, and the two blocks start to move with different angular velocities. Following that, numerous middle and base impacts occur, and the system changes continuosly its pattern until the system stops rocking. Finally, the system continues its motion in pattern 0, until it comes to rest.

5.1 | Overturning spectra: Constant period of the isolator

When the sine-pulse analysis is used to obtain overturning spectra, it can be an effective tool to understand the dynamic response of rocking systems. This type of spectra is created by subjecting the system to a wide range of sine pulses that differ in frequency and amplitude, and then determining whether or not overturning occurs. When a single rocking rigid block undergoes a sine-pulse ground motion, it can overturn in two manners: (a) with no impact and (b) following an impact between lower block and foundation (Dimitrakopoulos & DeJong, 2012). In this case, where two blocks are stacked one on top of the other, overturning can occur in any of the above-mentioned patterns and can involve a variety of impacts. The overturning mechanisms can be divided in four different types: (a) no impact; (b) middle impact, where an impact between the two blocks occurs; (c) base impact, in which the lower block impacts the base isolation device one or more times prior to the collapse; and (d) base and middle impact, where the two blocks impact one another and the lower block impacts with the isolator prior to the overturning.

Here, the investigated system (Figure 5a) is used to evaluate the performance of the isolator on the overall dynamic response. Three rocking spectra, for different periods T_b, are derived to study the effect of the isolation system (Figure 6). Overturning spectra are generally built by normalizing the frequency of the pulse with respect to the inverted pendulum frequency parameter, and the amplitude of the pulse by the minimum acceleration that triggers the rocking motion (Housner, 1963), also called the uplift acceleration. Because the upper block can be seen as the valuable object to be protected using the base isolation technique, its response can be used as a benchmark to evaluate the efficiency of the isolator and the influence of the other system parameters. Hence, the frequency parameter p_2 and the acceleration $g\tan(\alpha_2)$ (Equation 17), related to the upper block alone, are used. The analytical rocking spectra for the upper block alone are computed using the

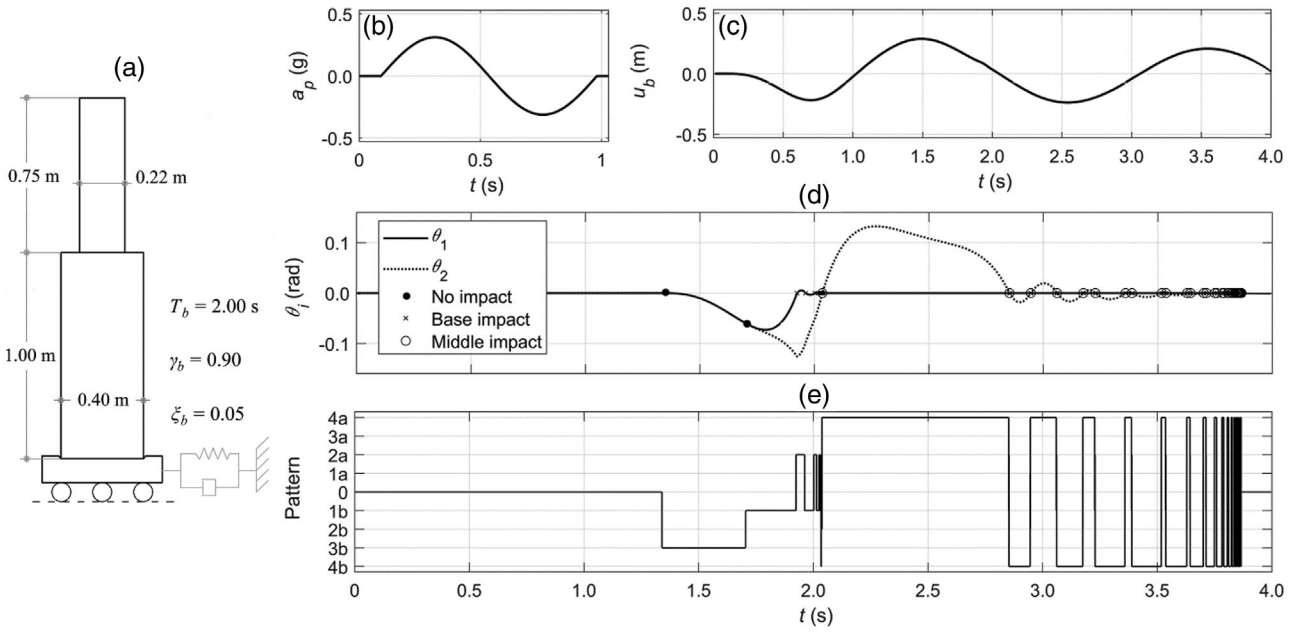

FIGURE 5 Response to sine-pulse ground motion of the reference system: (a) reference system: base isolation of a sculpture placed on a pedestal; (b) pulse-like ground motion time history; (c) displacement of the base isolation versus time; (d) rotations versus time; (e) pattern versus time.

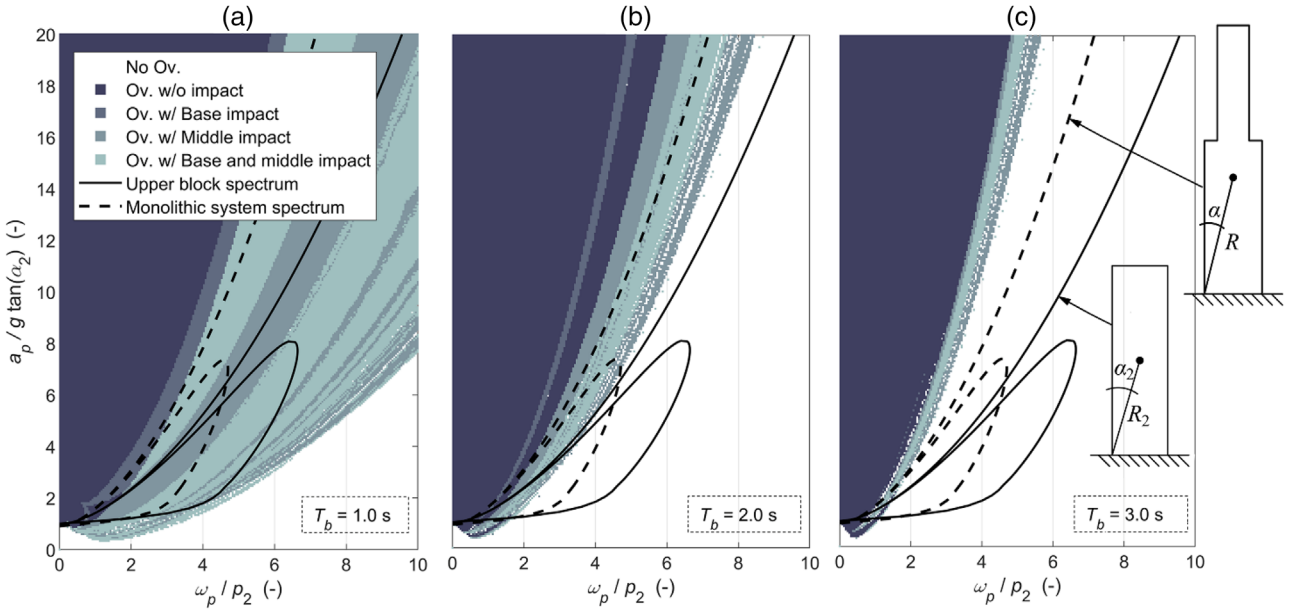

FIGURE 6 Rocking spectra (built assuming a constant isolator period) of the investigated system for various isolator periods: (a) $T_b = 1.0$ s; (b) $T_b = 2.0$ s; (c) $T_b = 3.0$ s.

equations in Dimitrakopoulos and DeJong (2012) and are shown with a black line in Figure 6.

The overturning spectra in Figure 6 show how strongly the period T_b influences the global response of the system: As T_b increases, the overturning area shrinks, implying that the efficiency of the base isolation device increases as well. If the overturning spectrum for short periods T_b (Figure 6a) is compared with the response of the upper block alone, the overturning area is larger than the analytical spectra, meaning that the addition of the isolator decreases the safety level of the art object. When T_b is increased (Figure 6b,c), the overturning area shrinks and is generally contained within the analytical spectrum, implying that the use of the seismic isolation device increases

the safety level of the system. This effect is particularly evident for large values of ω_p or small values of p_2. The beneficial effect provided from the isolator vanishes when ω_p is small (or p_2 is large), and in this region, an overturning area below the upper block spectrum is noticed (Figure 6). The base isolation device is ineffective in this region because the upper block alone overturns for larger sine-pulse amplitudes than the isolated system. This peculiar behavior indicates that the isolator amplifies the ground motion: This amplification depends on R_T, the ratio between the pulse period, T_p, and the period of the isolator, T_b. Similar conclusions can be drawn when the analytical rocking spectra for the nonisolated system, considered as monolithic, is compared with the response of the isolated system (Figure 6). In this case, the overturning area is contained within the analytical spectrum only when long period isolators are used (Figure 6c), implying that to increase the safety level of the system, it is necessary to use base isolation devices with longer period if compared with the case of the upper block alone. Indeed, if the two analytical spectra are compared (Figure 6), it is possible to observe that the addition of the pedestal improves the performance of the system for large blocks or small period pulses. This behavior is slightly reversed for small blocks or for large period pulses; indeed in this region, the analytical spectrum of the nonisolated monolithic system is just below the spectrum of the nonisolated upper block alone.

Shock spectra (Irvine, 2002) can be a powerful tool to enhance the understanding of the dynamic response of LMDS oscillators (such as the base isolation in this study). This type of spectra is created by subjecting the LMDS to a wide range of sine pulses that differ in frequency and amplitude, and then determining the ratio of the maximum (pos) or minimum (neg) LMDS acceleration and the amplitude of the pulse. A sample shock spectrum (Figure 7a) is built using a full sine-pulse ground motion and an LMDS oscillator with damping ratio $\xi_b = 0.05$, the same as in the linear isolator of the investigated system. The spectrum highlights how the LMDS system can amplify the ground motion, because the oscillator tends to become in phase with the second half of the full sine pulse. This phenomenon has a significant influence on the response of isolated rocking-block systems; the overturning spectrum of Figure 6b, after zooming in on the region below the analytical spectrum of the upper block (see Figure 7b), mimics a mirrored shock spectrum (Figure 7a). Further observations on the relationship between normalized minimum overturning acceleration and amplification of the LMDS system can be found in the following sections (Figure 11).

Shock spectra were also constructed using a half sine-pulse ground motion and an LMDS oscillator with varying damping factors (Figure 7c). The spectrum for $\xi_b =$ 0.05 shows smaller amplitudes compared with Figure 7a, because there is no synchronicity anymore between the response of the oscillator and the second half of the full sine pulse. Given the simpler nature of this spectrum, for which no minimum (negative) amplification is present any longer, it is possible to expand on the investigation of the damping effect. The shock spectra show how, as damping is increased, the amplification of the ground motion decreases in general. This behavior is weakly inverted for large damping factors and for long period pulses (or short LMDS oscillator periods). In this case, the beneficial effect of the damping vanishes, and the acceleration amplification can be slightly reduced for smaller values of the damping ratio (Figure 7c).

Finally, minimum acceleration rocking spectra (Figure 7d) for various damping factors and isolator periods are plotted. These spectra are built using only the first amplitude of the sine-pulse, which causes overturning, neglecting the information above this curve. The response of the system in Figure 7d for different damping ratios confirms the results obtained with the shock spectra (Figure 7c), indicating that as the damping ratio increases, so does the minimum acceleration necessary to overturn the system. Similar to the shock spectra, for large values of damping ratio and for large pulse circular frequency (or small frequency parameter p_2), the normalized minimum overturning acceleration decreases compared to the cases with smaller damping ratio. Observing, for example, the case with damping $\xi_b = 0.4$ in Figure 7d, it is possible to see that the curve, at approximately $\omega_p / p_2 = 1.25$, becomes almost straight and intersects the smaller damping curves. This behavior is due to the following: (a) The amplification of the LMDS oscillator becomes linear in this range of periods; (b) collapse occurs following only a middle impact (while in the previous stage, collapse occurs for both middle and base impacts). Thus, it is possible to conclude that adding damping to the isolator is generally beneficial for the system, but this may not be true for short period isolators with large damping. Moreover, when the period T_b is increased while keeping the damping constant, the area encompassed by the spectrum tends to shrink, but the minimum normalized accelerations of the spectra remain constant (Figure 7d).

5.2 | Overturning spectra: Constant period ratio

The previous rocking spectra in Figure 6 do not have the typical shape of a single rigid block rocking spectrum (Zhang & Makris, 2001), in which two areas can be distinguished: (a) a region where the overturning occurs without impact and (b) a bubble-shaped region where overturning

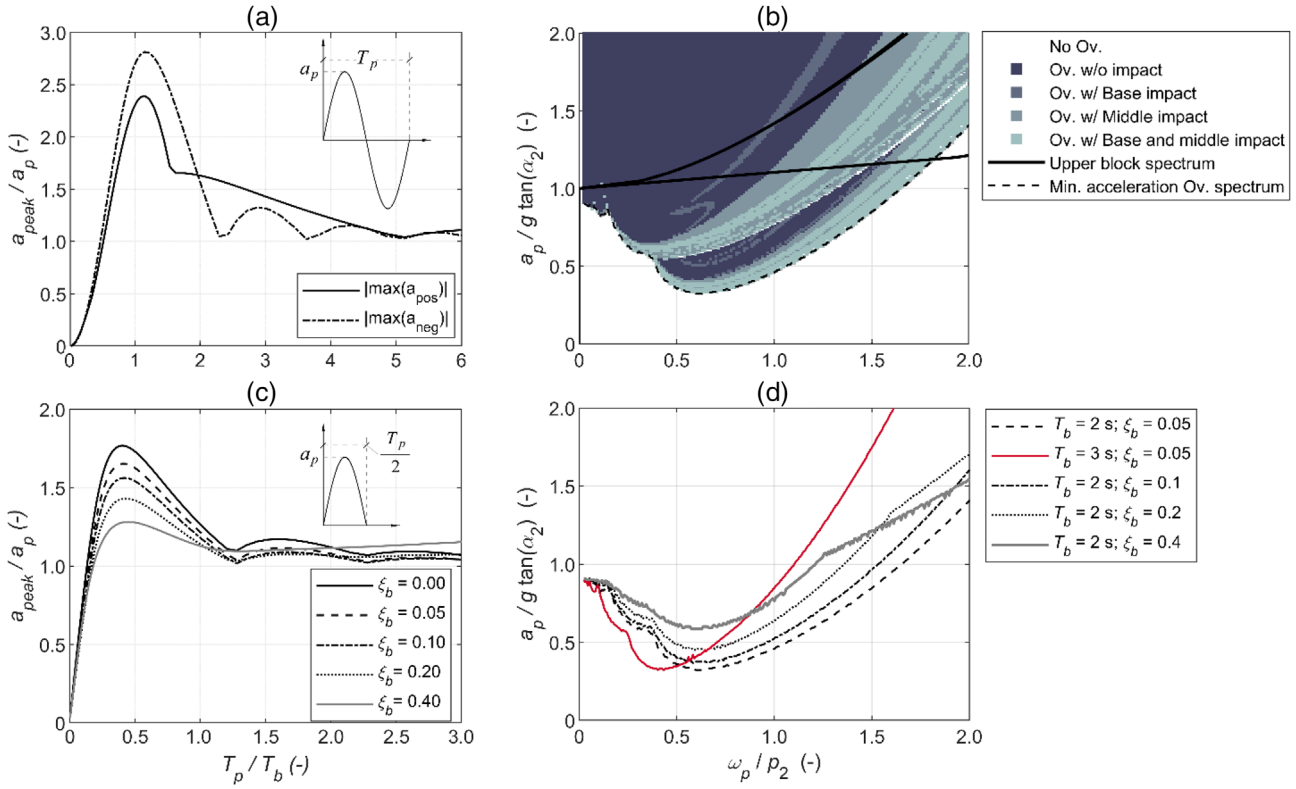

FIGURE 7 LMDS oscillator shock spectra for: (a) full sine-pulse ground motion; (b) detail of the overturning spectra in Figure 6b; (c) half sine-pulse ground motion for different damping ratios; (d) minimum acceleration overturning spectra for different base isolation damping ratios and periods.

occurs following an impact with the foundation. The reason for this difference can be found in the altering effect of the base isolation on the sine-pulse ground motion. As previously stated, the ratio R_T plays an important role in the response of the system; if the period of the base isolation is kept constant while building the rocking spectra, then R_T is allowed to vary. Thus, the amplification of the linear isolator is different for each step of the analysis, implying that the response is significantly altered when compared to the simple rigid block placed on a rigid foundation.

Alternatively, the rocking spectra can be built assuming that the period ratio R_T remains constant (Figure 8) for all analyses, which means that the amplification of the ground motion caused by the linear isolator remains constant. For these reasons, two distinct rocking spectra are built for two different period ratios: (1) $R_T = 3$ (Figure 8a) and (2) $R_T = 1/3$ (Figure 8b). The results in this case show that by keeping the ratio R_T constant during spectrum construction, the typical bubble-shaped rocking spectra (Vassiliou & Makris, 2012) and the distribution of the overturning mechanisms (Chatzis et al., 2018) are restored. When the two rocking spectra are compared, it is noticeable that the minimum overturning acceleration increases as the period ratio decreases. The reason for this behavior is again illuminated by the full sine-pulse shock spectrum (Figure 8c); indeed, the use of a constant period ratio implies that the amplification of the linear isolator is constant. If the period ratio is assumed to be 3, a_p is amplified by approximately 1.30 times, whereas if R_T is 1/3, the ground motion is amplified by approximately 0.55 times (i.e., deamplified). Finally, the rocking spectra are compared to the response of the upper block on a rigid foundation (expressed in terms of analytical spectra). The base isolation system is generally ineffective when $R_T = 3$, because the isolated system overturns for a smaller amplitude of the ground motion than the upper block alone. When R_T is assumed to be 1/3, the isolator appears to be effective for small values of ω_p (or for large values of p_2), but ineffective for small frequency pulses or blocks of large size (small values of p_2). The last observations lead to the conclusion that isolation technology may be ineffective in some circumstances (e.g., for short period pulses) in preventing overturning of rocking systems. However, it is important to note that the period T_b of the base isolation is different for each simulation when building this type of spectrum (Figure 8a,b). The use of isolators having a small period, for example, $T_b < 2.0$ s, is not frequent in practice and it is well known that large values are usually effective (Figure 7), although they require that larger displacements are accommodated.

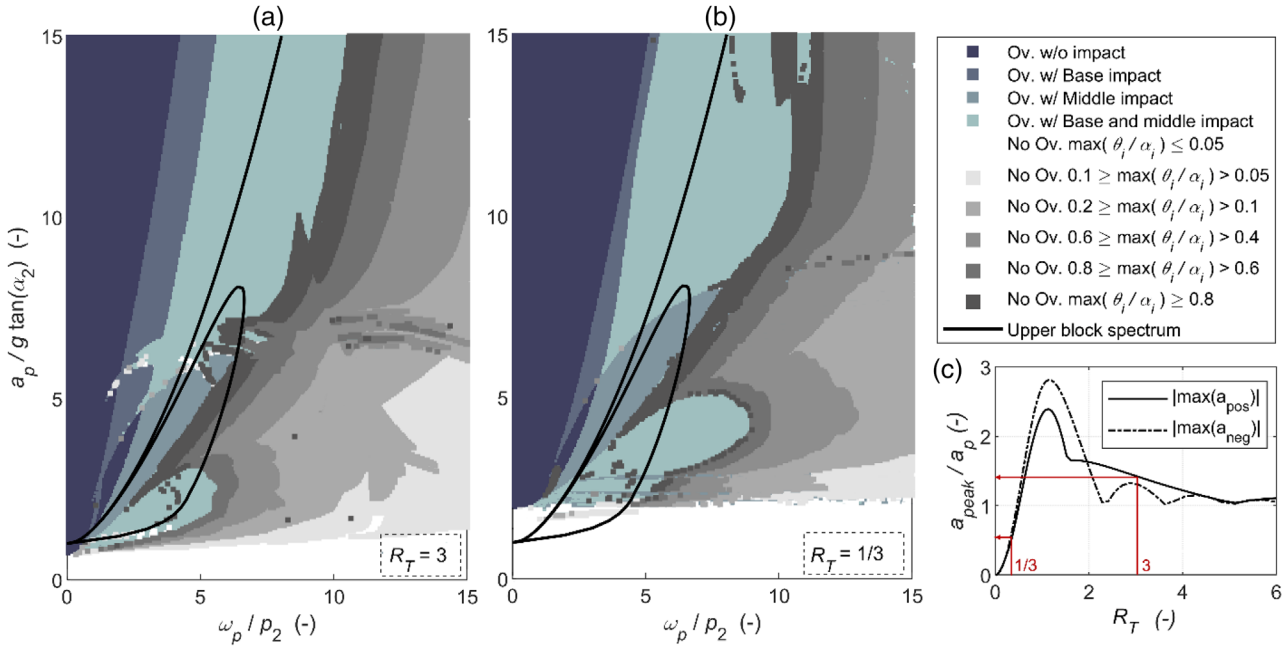

FIGURE 8 Rocking spectra of the investigated system for various period ratios R_T (assumed constant during the construction of every single spectrum): (a) $R_T = 3.0$; (b) $R_T = 1/3$; (c) LMDS oscillator shock spectra for the full sine-pulse ground motion and amplification for (a) and (b).

5.3 | Minimum acceleration overturning spectra: Normalization studies

Previously the effect of the period of the isolator on the global behavior of the system was investigated. The sine-pulse analysis and the minimum acceleration rocking spectra are used in the following sections to understand the influence of various system parameters. For this purpose, the use of minimum acceleration overturning spectra (built using only the minimum acceleration a_p that causes the overturning for each frequency) allows the response to be expressed with only one curve, making comparison easier. Furthermore, in this section, a novel normalization criterion is used to express the response of the system independent of the period of the isolator, and to investigate different parameters.

Here, 11 spectra are derived for 11 different T_b values (Figure 9), and the results confirm the previous observation: As the period increases, so does the safety level. When the spectra are built by normalizing the pulse frequency, ω_p, with respect to the frequency of the base isolation, ω_b, (rather than p_2), all the curves collapse into one. Consequently, it can be stated that (for a given value of p_2) by using the aforementioned normalization, the response of the system can be expressed independently of the period of the base isolation, facilitating the investigation of other parameters.

So far, normalization has always been referred to the upper block, with the goal of establishing the effectiveness of the base isolation system in protecting the upper rocking object; it is now necessary to evaluate the response of the system accounting (when necessary) for the presence of a lower block. The response is now evaluated in relation to two distinct slenderness values that characterize the system: (a) slenderness α of the two blocks considered as monolithic and (b) slenderness α_2 of the upper block alone. Further, the slenderness ratio R_α is introduced:

$$R_\alpha = \alpha_2 / \alpha \tag{19}$$

Therefore, different minimum acceleration overturning spectra are derived for various slenderness ratio values. In this case, the curves are built again for 11 periods to maintain independence from the period T_b, and the median values are assumed to define the spectrum of each different slenderness ratio. The amplitude of the pulse, a_p, is now normalized in two ways. First, it is normalized with respect to the slenderness of the monolithic system, α (Figure 10a), and then to the slenderness of the upper block alone, α_2 (Figure 10b). If the pulse amplitude is normalized with respect to α (Figure 10a), then the response of the system (when the slenderness ratio is greater than one) collapses into a single curve, whereas when $R_\alpha < 1$, the minimum acceleration for which overturning occurs decreases. On the other hand, if a_p is normalized with respect to α_2 (Figure 10b), the response of the system when $R_\alpha < 1$ collapses into one curve, while decreasing

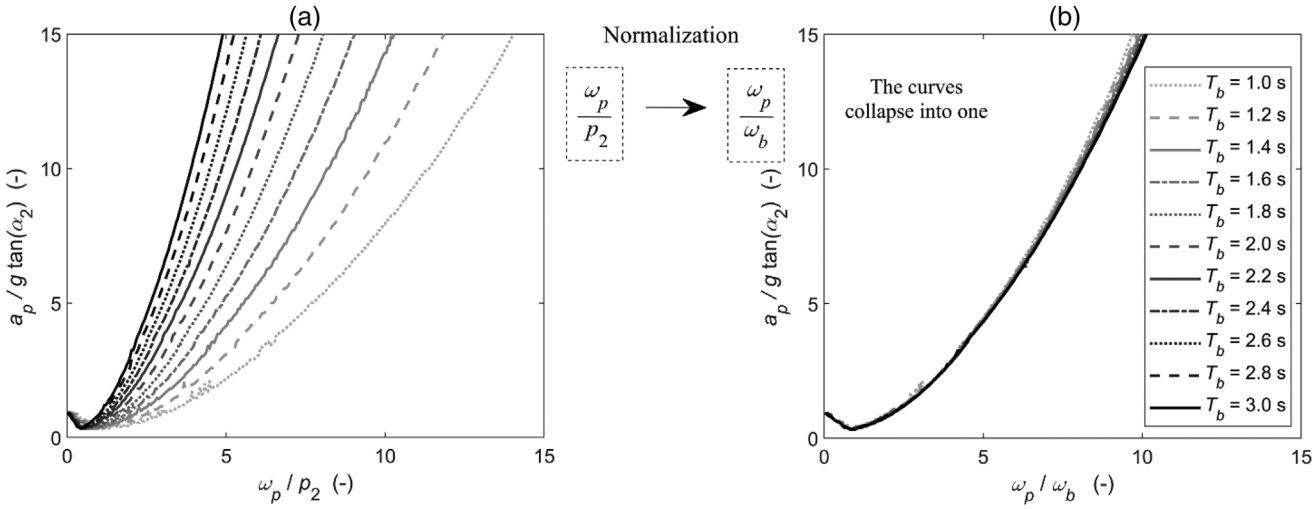

FIGURE 9 Minimum acceleration overturning spectra for 11 different isolator periods: a) pulse frequency normalized with respect to frequency parameter of the upper block; (b) pulse frequency normalized with respect to the frequency of the isolator.

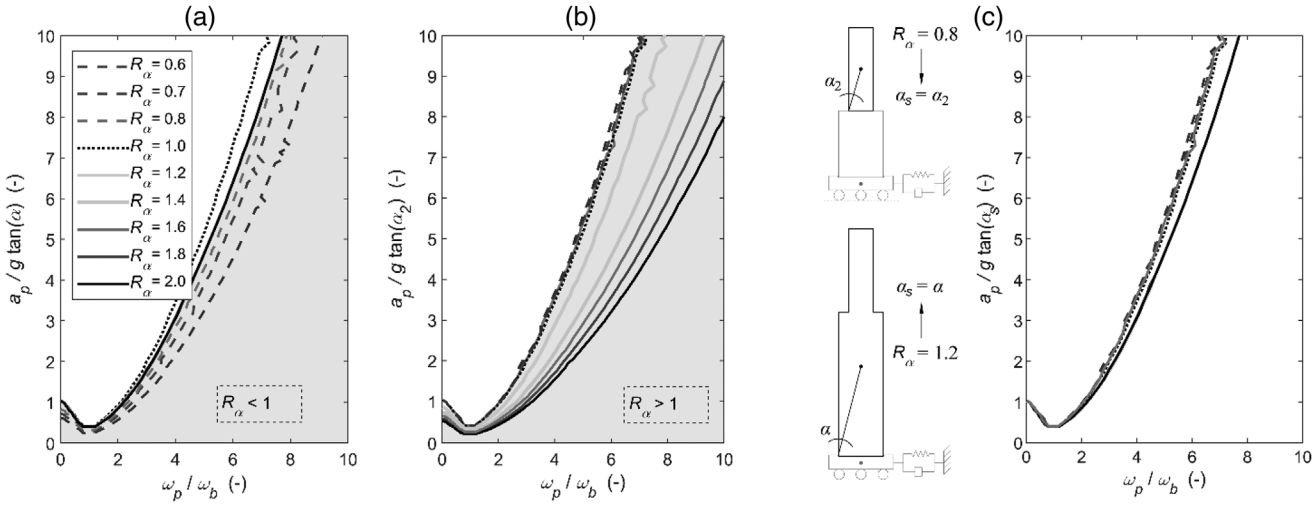

FIGURE 10 Minimum acceleration overturning spectra for different slenderness ratio: (a) pulse amplitude normalized with respect to the minimum uplift acceleration of the blocks considered monolithic; (b) pulse amplitude normalized with respect to the minimum uplift acceleration of the upper block alone; (c) pulse amplitude normalized with respect to the minimum uplift acceleration of the slenderest configuration.

the slenderness ratio ($R_\alpha > 1$), the minimum overturning acceleration decreases as well.

The results in Figure 10 highlight a useful phenomenon. The response of the system is governed by the slenderest configuration between (a) the whole system considered as monolithic and (b) the upper block alone. If the smaller slenderness is assumed to normalize the pulse amplitude, all the curves collapse into one (Figure 10c), allowing the response of the system to be described by considering only one slenderness parameter and ignoring the interaction between the two blocks. Thus, the slenderness α_s can be defined as in Equation (20). The same criterion can be applied to the frequency parameter of the system, and a parameter p_s can be defined in the same way as for α_s.

$$\begin{cases} \text{if } R_\alpha > 1 \rightarrow \alpha_2 > \alpha \rightarrow \alpha_s = \alpha;\ p_s = p \\ \text{if } R_\alpha < 1 \rightarrow \alpha_2 < \alpha \rightarrow \alpha_s = \alpha_2;\ p_s = p_2 \end{cases} \tag{20}$$

To validate the previous findings and to better understand the linear isolator amplification, the response in terms of shock spectra for an LMDS oscillator subjected to a full sine pulse is compared to the minimum acceleration overturning spectrum (Figure 11). Based on the results presented above, the spectra (Figure 11b) built for

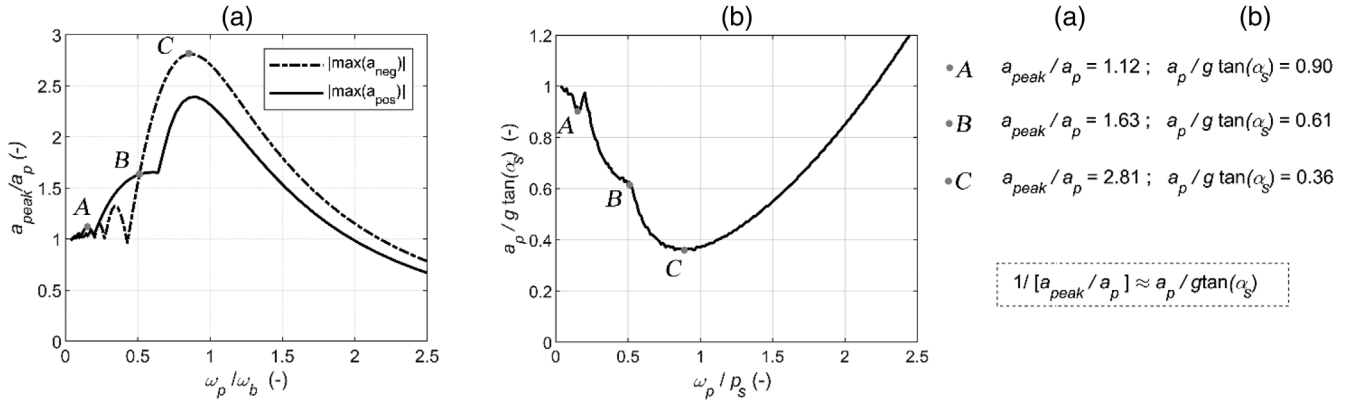

FIGURE 11 Comparison between the ground motion amplification of the LMDS oscillator and the normalized minimum overturning acceleration of the system: (a) LMDS oscillator shock spectra for the full sine-pulse ground motion in terms of frequencies; (b) minimum acceleration overturning spectra normalized with respect to the slenderest configuration.

the investigated system are normalized with respect to the slenderest configuration (the two blocks considered as monolithic in this case). Further, to facilitate comparisons, the shock spectrum (Figure 11a) is expressed in terms of the ratio between the frequency of the pulse and the frequency of the LMDS oscillator. When the two spectra are compared, the correlation between the dynamic amplification of the LMDS oscillator and the minimum nondimensional overturning acceleration is evident, especially now that the response of the system has been normalized with respect to the proper configuration. Thus, some specific peaks of the response are investigated for both spectra (points A, B, and C in Figure 11a,b) to prove the exact correspondence between the LMDS oscillator amplification and overturning acceleration. When the peak amplification (Figure 11a) is compared to the minimum overturning acceleration (Figure 11b) in points A, B, and C, it is possible to observe that these two values are approximately the reciprocal of each other.

These final observations lead to three considerations: (a) The minimum overturning acceleration is an exact function of the LMDS oscillator dynamic amplification, and it is governed by the ratio between the pulse frequency (period) and the frequency (period) of the linear isolator; (b) the final behavior depends on the envelope of the maximum response between the positive and negative amplification of the LMDS oscillator; and (c) the correspondence between α_s and a_{peak} further justifies the normalization with respect to the more slender configuration. Indeed, when the response of the system is normalized using the characteristics of the upper block (Figure 7b), it is possible to observe a slight difference between the minimum overturning acceleration and the amplification of the LMDS oscillator (Figure 11a).

The influence of the mass ratio γ_b on the response of the system is also investigated here; for this purpose, the response of the system varying the mass ratios is analyzed (Figure 12).

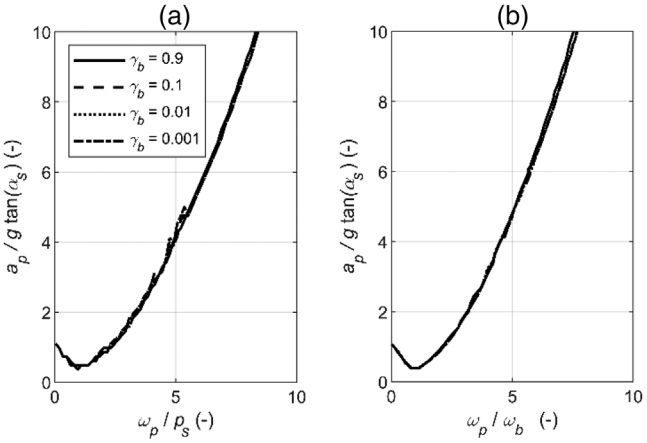

FIGURE 12 Minimum acceleration overturning spectra for different mass ratios: (a) pulse frequency normalized with respect to the frequency parameter of the slenderest configuration; (b) pulse frequency normalized with respect to the frequency of the isolator.

Minimum acceleration overturning spectra (Figure 12a) are obtained, assuming a constant value of $T_b = 2$ s, for various mass ratios ranging from $\gamma_b = 0.9$ (light isolator mass) to $\gamma_b = 0.001$ (very heavy isolator mass). The results show that this parameter has little effect on the response of the system, which remains approximately constant for different mass ratios.

The response of the system to different γ_b is then investigated for different periods of the base isolator (Figure 11b). As previously observed (Figure 8), if the pulse frequency is normalized with respect to the frequency of the base isolator, the normalized minimum acceleration overturning spectra collapse into one; the mass ratio has no effect also in this case, and the response is approximately the same for different T_b and different γ_b (Figure 12b). In

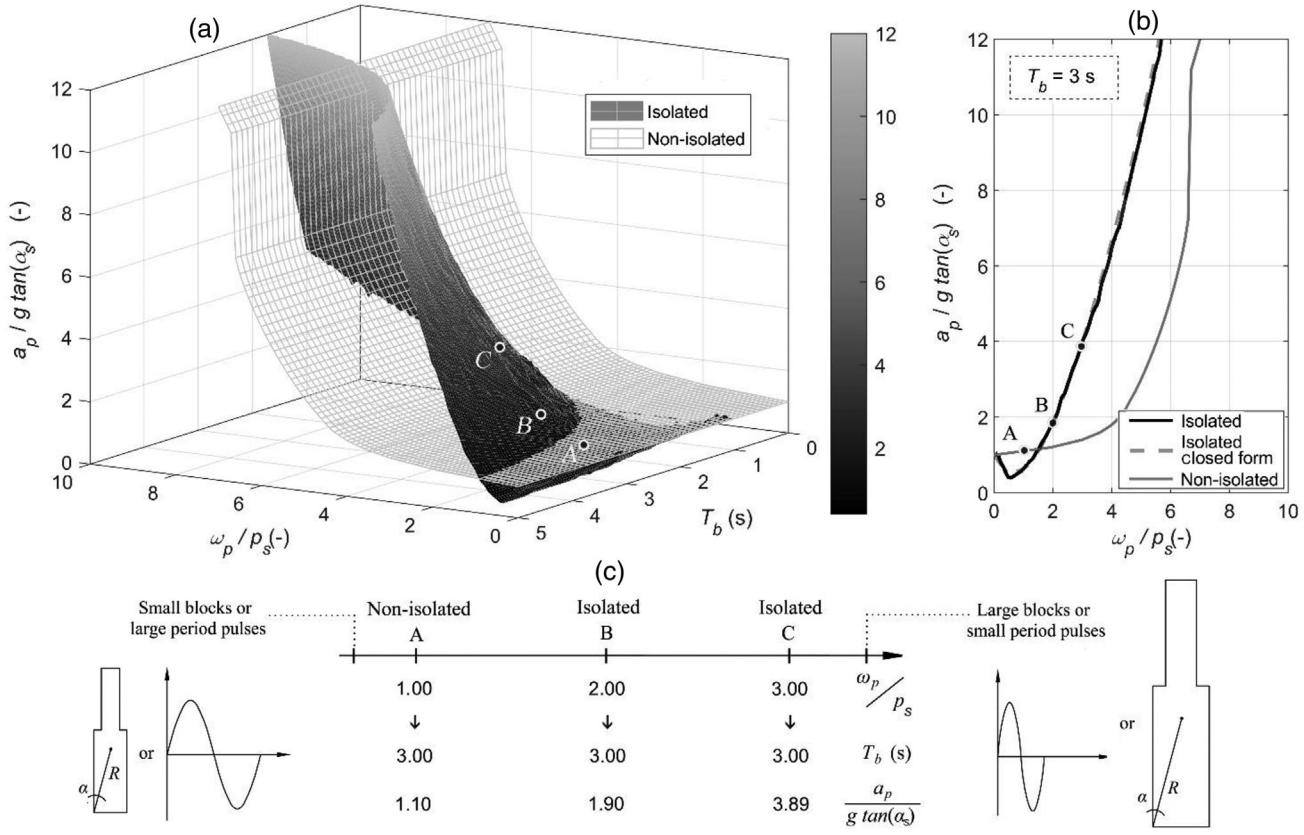

FIGURE 13 (a) Three-dimensional normalized minimum acceleration overturning spectra for the isolated and for the nonisolated system; (b) minimum acceleration overturning spectra for the isolated (for $T_b = 3.0$ s), numerical, and closed form, as well as for the nonisolated system; (c) values in terms of normalized pulse frequency, period of the isolator, and normalized minimum overturning acceleration for the points A, B, and C.

conclusion, the results indicate that the ratio between the mass of the blocks and the total mass (including the isolator) does not significantly influence the response.

Once the influence of parameters such as the damping ratio (Figure 7) and the mass ratio (Figure 12) is understood, and the response of the system is reduced to only one slenderness parameter α_s, a three-dimensional overturning spectrum is derived. The spectrum is built subjecting the system to a wide range of pulses that differ in amplitude and frequency, while also varying the period of the isolator. The spectrum (Figure 13a) confirms the previous observations, that is, that increasing the period of the isolator increases the safety level of the system. Figure 13 also shows the analytical overturning spectrum when the system is considered as monolithic and placed on a rigid foundation. The surface describing the response of the nonisolated system obviously does not depend on the period of the isolator, so it remains constant for any T_b. When the two surfaces, that is, the isolated and nonisolated responses, are compared, a region can be identified in which the response of the system standing on a rigid foundation is safer than when it is isolated. This region is larger for small periods T_b, where the isolation is almost ineffective, and it shrinks as the period of the isolator increases (as does the isolator efficiency). Further, the efficiency of the base isolation is determined not only by its period, but also by the frequency of the pulse and the frequency parameter of the rocking object.

Three cases are investigated here (points A, B, and C in Figure 13a,b), using the three-dimensional overturning spectrum (Figure 13a) and the two-dimensional overturning spectra (Figure 13b) for a constant period $T_b = 3.0$ s. In the case of a long period pulse or a small block (point A), the response of the system is safer in the nonisolated case; indeed, the amplification of the linear isolator is particularly evident in this region. Decreasing the pulse period or increasing the size of the block (point B) increases isolator effectiveness, and the isolated system becomes safer than the nonisolated. In the case of a large block or a short period pulse (point C), the beneficial effect of the base isolation device further increases, which means that the minimum overturning acceleration increases as well. The outcomes demonstrate that the dynamic response of the system is systematic. For this reason, the closed-form fit of

the overturning spectrum in Figure 13b can have practical applications, and it is presented as follows:

$$\frac{a_p}{g\ \tan(\alpha_s)} = 0.992 - 1.38\frac{\omega_p}{p_s} + 1.227\left(\frac{\omega_p}{p_s}\right)^2 - 0.176\left(\frac{\omega_p}{p_s}\right)^3 + 0.0114\left(\frac{\omega_p}{p_s}\right)^4 \quad (21)$$

To maximize efficiency of the base isolation technology, the response of the system should be moved as far away as possible from the region where the ground motion is amplified by the linear isolator. This outcome could be obtained by increasing the period of the isolator. For example, assuming $T_p = 0.8$ s (Makris, 2000) and $p = 3.1$ rad/s (as for the system in Figure 5a), the isolator is effective for $T_b > 2.0$ s. Nevertheless, for long period pulses or small blocks the minimum overturning acceleration of the isolated system can be lower than the nonisolated system. Assuming $T_p = 0.8$ s and using a very small block (i.e., a household brick for which $p \approx 8.0$ rad/s), the isolator becomes efficient only for $T_b > 5.0$ s. This potentially dangerous phenomenon disappears for small periods of the pulse or for large blocks. Indeed, assuming a large block (i.e., a computer server $p \approx 2.7$ rad/s) and considering the same period pulse of the previous example, the isolator becomes efficient for $T_b > 1.6$ s. Therefore, the safety level of the system may be enhanced by increasing the size of the lower block (pedestal) while keeping α_s constant. This solution might become impractical if the upper block needs to remain at a reasonable height, such as for an art object in an exhibition. In that case, a possible alternative is restraining the upper block to a squat lower block, but this solution might involve large internal stresses that may be incompatible with brittle historical artifacts (Sorace & Terenzi, 2015).

6 | CONCLUSION

A dynamic two rigid body rocking model isolated at the base was developed. The friction was assumed large enough to prevent any sliding, the two blocks can rock only about the corners and the impacts are assumed to be instantaneous. Then, the computational method used to solve the governing equations was presented in terms of pseudocode, emphasizing the events marking the transition between the five possible patterns.

The model was used to derive rocking spectra for two-block systems subjected to sine-pulse ground motion, described by its amplitude and frequency. The main findings, can be summarized as follows:

1. The base isolation device is effective for long period devices.
2. As an alternative or concurrent approach to the design of a long period device, the size of the system could be increased to enhance the effectiveness of the base isolation.
3. Depending on the size of the system, if long period pulses are expected, it could be impossible to deliver an effective base isolation with current technologies.
4. The amplification caused by the isolator depends on the ratio between the pulse period and the period of the isolator, and the amplification of the LMDS oscillator, which can be obtained using shock spectra for specific pulses, is the reciprocal of the normalized minimum overturning acceleration of the system.
5. Overturning spectra can be obtained assuming the isolator period to be constant or assuming a constant ratio of the periods (between the pulse and that of the isolator). The latter type of spectra must be carefully interpreted because each frequency of the pulse corresponds to a different isolator period, meaning that T_b is constantly varying along the x-axis.
6. Minimum overturning acceleration spectra can be used to describe the response of the system; when the frequency of the impulse is normalized with respect to the frequency of the isolator, the response for different isolator periods collapses to a single curve.
7. The response of two stacked rocking blocks can be understood using only one configuration, the slenderest between the two blocks considered as monolithic and the upper block alone. This means that, using the proper configuration, the response of the two-block system to sine-pulse ground motion can be approximated well by neglecting block interaction.

Potential future developments involve the consideration of alternative excitations, such as symmetric and antisymmetric Ricker wavelets and recorded accelerograms, in order to consider either more dangerous or more realistic excitations. Additionally, the no-sliding hypothesis and homogeneous density assumption could be removed, while configurations involving three or more bodies could be investigated.

ACKNOWLEDGMENTS

This work was partially carried out under the MONALISA research project funded by Lazio Regional Government and Italian Ministry of University and Research. The opinions expressed in this publication are those of the authors and are not necessarily endorsed by the funding bodies.

FUNDING INFORMATION

This work was partially carried out under the MONALISA (MONitoraggio Attivo e Isolamento da vibrazioni e Sismi di oggetti d'Arte = Active monitoring and

isolation from vibrations and earthquakes of art objects) research project funded by Lazio Regional Government and Italian Ministry of University and Research, project ID 305-2020-35576.

ORCID

Giacomo Destro Bisol https://orcid.org/0000-0002-1266-9065
Matthew DeJong https://orcid.org/0000-0002-6195-839X
Domenico Liberatore https://orcid.org/0000-0003-3184-8189
Luigi Sorrentino https://orcid.org/0000-0003-1652-942X

REFERENCES

AlShawa, O., Sorrentino, L., & Liberatore, D. (2017). Simulation of shake table tests on out-of-plane masonry buildings. Part (II): Combined finite-discrete elements. *International Journal of Architectural Heritage*, *11*(1), 79–93.

Amarante Dos Santos, F., & Fraternali, F. (2022). Novel magnetic levitation systems for the vibration control of lightweight structures and artworks. *Structural Control and Health Monitoring*, *29*(8), 1–14.

Baggio, S., Berto, L., Favaretto, T., Saetta, A., & Vitaliani, R. (2015). Seismic isolation technique of marble sculptures at the Accademia Gallery in Florence: Numerical calibration and simulation modelling. *Bulletin of Earthquake Engineering*, *13*(9), 2719–2744.

Baggio, S., Berto, L., Rocca, I., & Saetta, A. (2018). Vulnerability assessment and seismic mitigation intervention for artistic assets: From theory to practice. *Engineering Structures*, *167*, 272–286.

Bao, Y., & Konstantinidis, D. (2020). Dynamics of a sliding-rocking block considering impact with an adjacent wall. *Earthquake Engineering & Structural Dynamics*, *49*(5), 498–523.

Berto, L., Favaretto, T., & Saetta, A. (2013). Seismic risk mitigation technique for art objects: Experimental evaluation and numerical modelling of double concave curved surface sliders. *Bulletin of Earthquake Engineering*, *11*(5), 1817–1840.

Bitaraf, M., Hurlebaus, S., & Barroso, L. R. (2012). Active and semi-active adaptive control for undamaged and damaged building structures under seismic load. *Computer-Aided Civil and Infrastructure Engineering*, *27*(1), 48–64.

Caliò, I., & Marletta, M. (2003). Passive control of the seismic rocking response of art objects. *Engineering Structures*, *25*(8), 1009–1018.

Chatzis, M. N., García Espinosa, M., Needham, C., & Williams, M. S. (2018). Energy loss in systems of stacked rocking bodies. *Journal of Engineering Mechanics*, *144*(7), 04018044.

D'Angela, D., Magliulo, G., & Cosenza, E. (2021). Seismic damage assessment of unanchored nonstructural components taking into account the building response. *Structural Safety*, *93*, 102126.

D'Angela, D., Magliulo, G., & Cosenza, E. (2022). Incremental dynamic analysis of rigid blocks subjected to ground and floor motions and shake table protocol inputs. *Bulletin of the New Zealand Society for Earthquake Engineering*, *55*(2), 64–79.

Dar, A., Konstantinidis, D., & El-Dakhakhni, W W. (2016). Evaluation of ASCE 43-05 seismic design criteria for rocking objects in nuclear facilities. *Journal of Structural Engineering*, *142*(11), 4016110.

De Canio, G. (2012). Marble devices for the base isolation of the two Bronzes of Riace: a proposal for the David of Michelangelo. *15th world conference on earthquake engineering*, 22–29 September, 3098, Lisbon, Portugal.

DeJong, M. J., & Dimitrakopoulos, E. G. (2014). Dynamically equivalent rocking structures. *Earthquake Engineering & Structural Dynamics*, *43*(10), 1543–1563.

Destro Bisol, G., DeJong, M. J., Liberatore, D., & Sorrentino, L. (2023). Formulation of the post impact velocities for the seismically-isolated two-block system. Zenodo. https://doi.org/10.5281/zenodo.7839940

Diamantopoulos, S., Yanni, H., & Fragiadakis, M. (2022). Modeling of museum artifacts under seismic loading as two-block rocking systems. In G. Stavroulakis, D. Polyzos, & G. Hantzigeorgiou (Eds.), *13th Hellenic Society for Theoretical and Applied Mechanics International Congress on Mechanics*, 24-27 August 2022, Patras, Greece.

Dimitrakopoulos, E. G., & Dejong, M. J. (2012). Revisiting the rocking block: Closed-form solutions and similarity laws. *Proceedings of the Royal Society A: Mathematical, Physical and Engineering Sciences*, *468*(2144), 2294–2318.

Di Egidio, A., & Contento, A. (2009). Base isolation of slide-rocking non-symmetric rigid blocks under impulsive and seismic excitations. *Engineering Structures*, *31*(11), 2723–2734.

Di Egidio, A., Contento, A., De Leo, A. M., & Gardoni, P. (2020a). Dynamic and seismic protection of rigid-block-like elements and structures on deformable ground with mass-damper dynamic absorbers. *Journal of Engineering Mechanics*, *146*(6), 4020046.

Di Egidio, A., Contento, A., Olivieri, C., & Leo, A. M. (2020b). Protection from overturning of rigid block-like objects with linear quadratic regulator active control. *Structural Control and Health Monitoring*, *27*(10), e2598.

Di Sarno, L., Magliulo, G., D'Angela, D., & Cosenza, E. (2019). Experimental assessment of the seismic performance of hospital cabinets using shake table testing. *Earthquake Engineering & Structural Dynamics*, *48*(1), 103–123.

El-Khoury, O., & Adeli, H. (2013). Recent advances on vibration control of structures under dynamic loading. *Archives of Computational Methods in Engineering*, *20*(4), 353–360.

Fabien, B. (2008). *Analytical system dynamics: Modeling and simulation*. Springer.

Fantuzzi, N., Rustico, A., Formenti, M., & Ferreira, A. J. M. (2022). 3D active dynamic actuation model for offshore cranes. *Computer-Aided Civil and Infrastructure Engineering*, *37*(7), 864–877.

Fragiadakis, M., & Diamantopoulos, S. (2020). Fragility and risk assessment of freestanding building contents. *Earthquake Engineering & Structural Dynamics*, *49*(10), 1028–1048.

Fragiadakis, M., DiSarno, L., Saetta, A., Castellano, M. G., Rocca, I., Diamantopoulos, S., Crozet, V., Politopoulos, I., Chaudat, T., Vasic, S., Bal, I. E., Smyrou, E., Psycharis, I., Hutchinson, T. C., & Berto, L. (2020). Experimental seismic assessment and protection of museum artefacts. In M. Papadrakakis, M. Fragiadakis, C. Papadimitriou (Eds.), *EURODYN 2020 XI International Conference on Structural Dynamics*, 23-26 November 2020, Athens, Greece. EASD Procedia.

Froli, M., Giresini, L., & Laccone, F. (2019). Dynamics of a new seismic isolation device based on tribological smooth rocking (TROCKSISD). *Engineering Structures*, *193*, 154–169.

Ghaedi, K., Ibrahim, Z., Adeli, H., & Javanmardi, A. (2017). Invited review: Recent developments in vibration control of building

and bridge structures. *Journal of Vibroengineering*, *19*(5), 3564–3580.

Giouvanidis, A. I., & Dimitrakopoulos, E. G. (2018). Rocking amplification and strong-motion duration. *Earthquake Engineering & Structural Dynamics*, *47*(10), 2094–2116.

Gutierrez Soto, M., & Adeli, H. (2017). Many-objective control optimization of high-rise building structures using replicator dynamics and neural dynamics model. *Structural and Multidisciplinary Optimization*, *56*, 1521–1537.

Gutierrez Soto, M., & Adeli, H. (2018). Vibration control of smart base-isolated irregular buildings using neural dynamic optimization model and replicator dynamics. *Engineering Structures*, *156*, 322–336.

Gutierrez Soto, M., & Adeli, H. (2019). Semi-active vibration control of smart isolated highway bridge structures using replicator dynamics. *Engineering Structures*, *186*, 536–552.

Higashino, M., & Okamoto, S. (2006). *Response control and seismic isolation of buildings*. Taylor and Francis.

Housner, G. W. (1963). The behavior of inverted pendulum structures during earthquakes. *Bulletin of the Seismological Society of America*, *53*(2), 403–417.

Housner, G. W., Soong, T. T., & Masri, S. F. (1996). Second generation of active structural control in civil engineering. *Computer-Aided Civil and Infrastructure Engineering*, *11*(5), 289–296.

Huang, B., Günay, S., & Lu, W. (2022). Seismic assessment of freestanding ceramic vase with shaking table testing and performance-based earthquake engineering. *Journal of Earthquake Engineering*, *26*(15), 7956–7978.

Humar, J. (1990). *Dynamics of structures*. Prentice-Hall.

Irvine, T. (2002). *An introduction to the shock response spectrum*. Vibrationdata. https://www.vibrationdata.com/tutorials2/srs_intr.pdf. Last consulted on 18 April, 2023

Javidan, M. M., & Kim, J. (2022). Fuzzy-based method for efficient seismic performance evaluation of structures with uncertainty. *Computer-Aided Civil and Infrastructure Engineering*, *37*(6), 781–802.

Kayabekir, A. E., Nigdeli, S. M., & Bekdaş, G. (2022). A hybrid metaheuristic method for optimization of active tuned mass dampers. *Computer-Aided Civil and Infrastructure Engineering*, *37*(8), 1027–1043.

Kim, H., & Adeli, H. (2005a). Hybrid control of smart structures using a novel wavelet-based algorithm. *Computer-Aided Civil and Infrastructure Engineering*, *20*(1), 7–22.

Kim, H., & Adeli, H. (2005b). Wavelet-hybrid feedback linear mean squared algorithm for robust control of cable-stayed bridges. *Journal of Bridge Engineering*, *10*(2), 116–123.

Kim, H., & Adeli, H. (2005c). Hybrid control of irregular steel high-rise building structures under seismic excitations. *International Journal for Numerical Methods in Engineering*, *63*(12), 1757–1774.

Kounadis, A. N. (2018). The effect of sliding on the rocking instability of multi-rigid block assemblies under ground motion. *Soil Dynamics and Earthquake Engineering*, *104*, 1–14.

Kuo, K., Suzuki, Y., Katsuragi, S., & Yao, G. C. (2011). Shake table tests on clutter levels of typical medicine shelves and contents subjected to earthquakes. *Earthquake Engineering & Structural Dynamics*, *40*(12), 1367–1386.

Li, Z., & Adeli, H. (2018). Control methodologies for vibration control of smart civil and mechanical structures. *Expert systems*, *35*(6), e12354.

Lin, C.-C., & Chen, C.-L., Wang, J.-F. (2010). Vibration control of structures with initially accelerated passive tuned mass dampers under near-fault earthquake excitation. *Computer-Aided Civil and Infrastructure Engineering*, *25*(1), 69–75.

Lourenço, P. B., Mendes, N., Ramos, L. F., & Oliveira, D. V. (2011). Analysis of masonry structures without box behavior. *International Journal of Architectural Heritage*, *5*(4–5), 369–382.

Makris, N. (2000). *Rocking response and rocking response and overturning of anchored equipment under seismic excitations*. Final Report to PG & E.

Malomo, D., Mehrotra, A., & DeJong, M. J. (2021). Distinct element modeling of the dynamic response of a rocking podium tested on a shake table. *Earthquake Engineering & Structural Dynamics*, *50*(5), 1469–1475.

MATLAB. (2018). *9.7.0.1190202 (R2019b)*. The MathWorks Inc.

Meirovitch, L. (1970). *Methods of analytical dynamics*. McGraw-Hil.

Naderpoor, P., & Taghikhany, T. (2022). Seismic adaptive control of building structures with simultaneous sensor and damper faults based on dynamic neural network. *Computer-Aided Civil and Infrastructure Engineering*, *37*(11), 1402–1416.

Naeim, F., & Kelly, J. M. (1999). *Design of seismic isolated structures: From theory to practice*. John Wiley & Sons.

Narasimhan, S., Nagarajaiah, S., Johnson, E. A., & Gavin, H. P. (2006). Smart base-isolated benchmark building. Part I: Problem definition. *Structural Control and Health Monitoring*, *13*(2-3), 573–588.

Noureldin, M., Ali, A., Nasab, M. S. E., & Kim, J. (2021). Optimum distribution of seismic energy dissipation devices using neural network and fuzzy inference system. *Computer-Aided Civil and Infrastructure Engineering*, *36*(10), 1306–1321.

Pellecchia, D., Lo Feudo, S., Vaiana, N., Dion, J., & Rosati, L. (2022). A procedure to model and design elastomeric-based isolation systems for the seismic protection of rocking art objects. *Computer-Aided Civil and Infrastructure Engineering*, *37*, 1298–1315.

Pellecchia, D., Sessa, S., Vaiana, N., & Rosati, L. (2020). Comparative assessment on the rocking response of seismically base-isolated rigid blocks. *Procedia Structural Integrity*, *29*, 95–102.

Prajapati, S., Destro Bisol, G., Alshawa, O., & Sorrentino, L. (2022). Non-linear dynamic model of a two-bodies vertical spanning wall elastically restrained at the top. *Earthquake Engineering & Structural Dynamics*, *51*(11), 2627–2647.

Prota, A., Zito, M., D'angela, D., Toscano, G., Ceraldi, C., Fiorillo, A., & Magliulo, G. (2022). Preliminary results of shake table tests of a typical museum display case containing an art object. *Advances in Civil Engineering*, *2022*, 1–18.

Psycharis, I. N. (1990). Dynamic behaviour of rocking two-block assemblies. *Earthquake Engineering & Structural Dynamics*, *19*(4), 555–575.

Roussis, P. C., Pavlou, E., & Pisiara, E. (2008). Base-isolation technology for earthquake protection of art objects. In *14th World Conference on Earthquake Engineering: Innovation Practice Safety*, 1990.

Saleh, A., & Adeli, H. (1998). Optimal control of adaptive/smart multistory building structures. *Computer-Aided Civil and Infrastructure Engineering*, *13*(6), 389–403.

Salvatore, A., Carboni, B., & Lacarbonara, W. (2021). Nonlinear dynamic response of an isolation system with superelastic hysteresis and negative stiffness. *Nonlinear Dynamics*, *107*(2), 1765–1790.

Shabana, A. A. (1997). Flexible multibody dynamics: review of past and recent developments. *Multibody System Dynamics*, *1*(2), 189–222.

Shi, X., Zhao, F., Yan, Z., Zhu, S., & Li, J.-Y. (2021). High-performance vibration isolation technique using passive negative stiffness and semiactive damping. *Computer-Aided Civil and Infrastructure Engineering*, *36*(8), 1034–1055.

Sorace, S., & Terenzi, G. (2015). Seismic performance assessment and base-isolated floor protection of statues exhibited in museum halls. *Bulletin of Earthquake Engineering*, *13*, 1873–1892.

Sorrentino, L., Alshawa, O., & Decanini, L. D. (2011). The relevance of energy damping in unreinforced masonry rocking mechanisms. Experimental and analytic investigations. *Bulletin of Earthquake Engineering*, *9*, 1617–1642.

Sorrentino, L., Masiani, R., & Griffith, M. C. (2008). The vertical spanning strip wall as a coupled rocking rigid body assembly. *Structural Engineering and Mechanics*, 29(4), 433–453.

Spanos, P. D., Roussis, P. C., & Politis, N. P. A. (2001). Dynamic analysis of stacked rigid blocks. *Soil Dynamics and Earthquake Engineering*, *21*(7), 559–578.

Vassiliou, M. F., & Makris, N. (2012). Analysis of the rocking response of rigid blocks standing free on a seismically isolated base. *Earthquake Engineering & Structural Dynamics*, *41*(2), 177–196.

Venanzi, I., Ierimonti, L., & Materazzi, A. L. (2020). Active base isolation of museum artifacts under seismic excitation. *Journal of Earthquake Engineering*, *24*(3), 506–527.

Vlachakis, G., Giouvanidis, A. I., Mehrotra, A., & Lourenço, P. B. (2021). Numerical block-based simulation of rocking structures using a novel universal viscous damping model. *Journal of Engineering Mechanics*, *147*(11), 4021089.

Xu, Y., Lu, X., Cetiner, B., & Taciroglu, E. (2021). Real-time regional seismic damage assessment framework based on long short-term memory neural network. *Computer-Aided Civil and Infrastructure Engineering*, *36*(4), 504–521.

Yim, C. S., Chopra, A. K., & Penzien, J. (1980). Rocking response of rigid blocks to earthquakes. *Earthquake Engineering & Structural Dynamics*, *8*(6), 565–587.

Zhang, J., & Makris, N. (2001). Rocking response of free-standing blocks under cycloidal pulses. *Journal of Engineering Mechanics*, *127*(5), 473–483.

How to cite this article: Destro Bisol, G., DeJong, M., Liberatore, D., & Sorrentino, L. (2023). Analysis of seismically-isolated two-block systems using a multi–rocking-body dynamic model. *Computer-Aided Civil and Infrastructure Engineering*, 1–22. https://doi.org/10.1111/mice.13012

APPENDIX A

Here, for brevity, only the equation of motion for pattern 1 (Figure 2) is described, as an example of a pattern with three DOFs. Once the equations of motion are obtained deriving the Lagrangian equation, they can be expressed in matrix form as follows:

$$\mathbf{M}\,\ddot{\mathbf{q}} = \mathbf{F};\ \begin{bmatrix} M_{11} & M_{12} & M_{13} \\ M_{21} & M_{22} & M_{23} \\ M_{31} & M_{32} & M_{33} \end{bmatrix} \cdot \begin{Bmatrix} \ddot{\theta}_1 \\ \ddot{\theta}_2 \\ \ddot{u}_b \end{Bmatrix} = \begin{Bmatrix} F_1 \\ F_2 \\ F_3 \end{Bmatrix}$$

where $\mathbf{M}$ is the mass matrix, $\ddot{\mathbf{q}}$ is the generalized coordinates acceleration vector, and $\mathbf{F}$ is the vector where the known terms and the low-order derivative, such as velocities and displacements, are contained. M_{jk} and F_k for pattern 1 are described next. The mass terms are defined as follows:

$$\begin{aligned} M_{11} &= I_{G1} + h_1^2 m_1 - 2b_1 b_2 m_2 + b_2^2 m_2 \\ &\quad + 4h_1^2 m_2 + b_1^2 m \\ M_{12} &= M_{21} = m_2\big(\big(b_1 b_2 - b_2^2 + 2h_1 h_2\big)\cos(\theta_1 - \theta_2) \\ &\quad + S_\theta(b_1 h_2 - b_2(2h_1 + h_2))\sin(\theta_1 - \theta_2)\big) \\ M_{13} &= M_{31} = (h_1)(2m_2 - m_1)\cos(\theta_1) \\ &\quad + S_\theta(b_2 m_2 - b_1 m)\sin(\theta_1) \\ M_{22} &= I_{G2} + \big(b_2^2 + h_2^2\big)m_2; M_{33} = m + m_b \\ M_{23} &= M_{32} = -m_2 h_2 \cos(\theta_2) - S_\theta(b_2 m_2 \sin(\theta_2)) \end{aligned}$$

where S_θ is the sign function:

$$S_\theta = 1 \text{ if } \theta > 0 \text{ or } S_\theta = -1 \; if \; \theta < 0$$

where $\theta \equiv \theta_1$ for patterns 1, 2, and 3, while $\theta \equiv \theta_2$ for pattern 4.

Vector $\mathbf{F}$ has the following components:

$$\begin{aligned} F_1 &= m_2\,(S_\theta(+b_1 h_2 - b_2(2h_1 + h_2))\ \cos(\theta_1 - \theta_2) \\ &\quad - \big(b_1 b_2 - b_2^2 + 2h_1 h_2\big)\ \sin(\theta_1 - \theta_2))\,\dot{\theta}_2^2 \\ &\quad + (h_1(m_1 + 2m_2)\ \cos(\theta_1) \\ &\quad - S_\theta(b_2 m_2 - b_1 m)\ \sin(\theta_1))\,\ddot{x}_g \\ &\quad + (S_\theta(b_2 m_2 - b_1 m)\ \cos(\theta_1) \\ &\quad + h_1(m_1 + 2m_2)\sin(\theta_1))(\ddot{y}_g + g) \\ F_2 &= m_2\ (S_\theta(b_2(2h_1 + h_2) - b_1 h_2)\ \cos(\theta_1 - \theta_2) \\ &\quad + \big(b_1 b_2 - b_2^2 + 2h_1 h_2\big)\ \sin(\theta_1 - \theta_2))\,\dot{\theta}_1^2 \\ &\quad + S_\theta(b_2 m_2\ \sin(\theta_2) - m_2 h_2\ \cos(\theta_2))\ddot{x}_g \\ &\quad + (m_2 h_2\ \sin(\theta_2) - S_\theta m_2 b_2\ \cos(\theta_2))(\ddot{y}_g + g) \end{aligned}$$

$$F_3 = (S_\theta(b_1 m - b_2 m_2)\cos(\theta_1) - h_1(m_1 + 2m_2)\sin(\theta_1))\dot{\theta}_1^2 + (S_\theta b_2 m_2 \cos(\theta_2) - h_2 m_2 \sin(\theta_2))\dot{\theta}_1^2 - c_b \dot{u}_b^2 - u_b k_b - (m + m_b)\ddot{x}_g$$

The equations of motion, obtained using the variational principle, are second-order differential equations, but the employed numerical integration procedure requires to reduce the problem to a first-order differential equation. In case of pattern 1 (applicable also for pattern 2), the state vector $\mathbf{y}$ can be expressed as follows:

$$y = \begin{Bmatrix} y(1) \\ y(2) \\ y(3) \\ y(4) \\ y(5) \\ y(6) \end{Bmatrix} = \begin{Bmatrix} \theta_1 \\ \dot{\theta}_1 \\ \theta_2 \\ \dot{\theta}_2 \\ u \\ \dot{u} \end{Bmatrix}$$

Using the time derivative vector $\dot{\mathbf{y}}$, the equations of motion can be reassembled as:

$$\begin{Bmatrix} 1 & 0 & 0 & 0 & 0 & 0 \\ 0 & M_{11} & 0 & M_{12} & 0 & M_{13} \\ 0 & 0 & 1 & 0 & 0 & 0 \\ 0 & M_{21} & 0 & M_{22} & 0 & M_{23} \\ 0 & 0 & 0 & 0 & 1 & 0 \\ 0 & M_{31} & 0 & M_{32} & 0 & M_{33} \end{Bmatrix} \begin{Bmatrix} \dot{y}(1) \\ \dot{y}(2) \\ \dot{y}(3) \\ \dot{y}(4) \\ \dot{y}(5) \\ \dot{y}(6) \end{Bmatrix} = \begin{Bmatrix} y(2) \\ F_1 \\ y(4) \\ F_2 \\ y(6) \\ F_3 \end{Bmatrix}$$

APPENDIX B

Here, a pattern change due to acceleration thresholds exceeded is investigated. For conciseness, only the pattern change from 3a to 1a is reported. In this case, the threshold acceleration that causes the pattern change is defined as follows:

$$\ddot{x}_{3,1} = (\ddot{\theta} I_{G2} + (2h_1 + h_2)(-(b_2\dot{\theta}^2) + \ddot{\theta}h_2)m_2 + b_1(b_2\ddot{\theta} + \dot{\theta}^2 h_2)m_2 + m_2(-(\ddot{u}_b h_2) + b_2(g + \ddot{y}_g))\cos(\theta) - m_2(b_2\ddot{u}_b + h_2(g + \ddot{y}_g))\sin(\theta))/(m_2(h_2\cos(\theta) + b_2\sin(\theta))).$$

Further, all the possible pattern changes due to acceleration thresholds exceeded are listed in Table B1.

TABLE B1 Pattern change due to acceleration thresholds exceeded.

From	Event	To	From	Event	To
3a	$\ddot{x}_{3,1} \le \ddot{x}_g(t)$	1a	3b	$\ddot{x}_{3,1} \ge \ddot{x}_g(t)$	1b
3a	$\ddot{x}_{3,2} \ge \ddot{x}_g(t)$	2a	3b	$\ddot{x}_{3,2} \le \ddot{x}_g(t)$	2b
4a	$\ddot{x}_{4,1} \le \ddot{x}_g(t)$	1a	4b	$\ddot{x}_{4,1} \ge \ddot{x}_g(t)$	1b
4a	$\ddot{x}_{4,2} \ge \ddot{x}_g(t)$	2b	4b	$\ddot{x}_{4,2} \le \ddot{x}_g(t)$	2a
0	$\ddot{x}_{0,3} \le \ddot{x}_g(t)$	3a	0	$\ddot{x}_{0,3} \ge \ddot{x}_g(t)$	3b
0	$\ddot{x}_{0,4} \le \ddot{x}_g(t)$	4a	0	$\ddot{x}_{0,4} \ge \ddot{x}_g(t)$	4b

APPENDIX C

As previously observed, during the motion of the system, impacts can occur implying a change in pattern. In this section, all the possible pattern changes due to impacts are listed. Following any kind of impact, the system can switch toward two different pattern categories: (a) primary, where the two blocks are moving with different velocities; and (b) secondary, where the lower block is at rest or the system is moving monolithically (interface between upper and lower block is closed). As described in Table C1, for all possible (positive) pattern changes, it is necessary to evaluate the postimpact velocities for the primary transition (type a), then a kinematic check is performed to exclude the possibility of interpenetration between the two blocks. If the kinematic control is not satisfied, the secondary pattern change (type b) must be used.

The postimpact velocities can be obtained solving the linear system in Equation (14). Especially for the cases where three DOFs are involved, the governing equations are large, hence only one pattern transition is described here with respect to the investigated system and for specific rotations. The postimpact velocities for every possible pattern change are presented in Destro Bisol et al. (2023). The transition from pattern 2a (2b) to pattern 1b (1a) is studied here. In this pattern change, the lower body impacts with the base isolation and the rotation of the lower block is 0, while the upper block has negative (positive) rotation.

The postimpact velocities are calculated for two different values of the upper block rotation. In the former, $\theta_2 = -0.001$ rad is assumed, while in the latter $\theta_2 = -0.100$ rad is assumed. The postimpact velocities, for the former (left) and for the latter case (right), can be calculated as:

$$\begin{cases} \dot{\theta}_1^+ = 0.330\dot{\theta}_1^- \\ \dot{\theta}_2^+ = \dot{\theta}_2^- + 0.518\dot{\theta}_1^- \\ \dot{u}_b^+ = \dot{u}_b^- - 0.684\dot{\theta}_1^- \end{cases}; \quad \begin{cases} \dot{\theta}_1^+ = 0.246\dot{\theta}_1^- \\ \dot{\theta}_2^+ = \dot{\theta}_2^- + 0.758\dot{\theta}_1^- \\ \dot{u}_b^+ = \dot{u}_b^- - 0.731\dot{\theta}_1^- \end{cases}$$

Although not the central scope of this work, some observations on the previous equations can be made. The velocity reduction of the isolator depends only on the

TABLE C1 Pattern change due to impacts.

From	Event	To	Kinematic assumption check		Assumption	To
1a	$\theta_1 = \theta_2$	2a	$\dot{\theta}_1^+ > \dot{\theta}_2^+$	false →	$\dot{\theta}_1^+ = \dot{\theta}_2^+$	3a
2a	$\theta_1 = \theta_2$	1a	$\dot{\theta}_1^+ < \dot{\theta}_2^+$	false →	$\dot{\theta}_1^+ = \dot{\theta}_2^+$	3a
4a	$\theta_1 = \theta_2$	1b	$\dot{\theta}_1^+ < 0$	false →	$\dot{\theta}_1^+ = 0$	4b
1a	$\theta_1 = 0$	2b	$\dot{\theta}_1^+ < 0$	false →	$\dot{\theta}_1^+ = 0$	4a
2a	$\theta_1 = 0$	1b	$\dot{\theta}_1^+ < 0$	false →	$\dot{\theta}_1^+ = 0$	4b
3a	$\theta_1 = 0$	1b	$\dot{\theta}_1^+ > \dot{\theta}_2^+$	false →	$\dot{\theta}_1^+ = \dot{\theta}_2^+$	3b

preimpact angular velocity of the lower block. Similarly to what was observed by Psycharis (1990) for this type of pattern change of two stacked blocks on a rigid foundation, the variation of angular velocity of the lower block is in general a reduction and this is large in comparison with the single block on a rigid foundation (Housner, 1963). Further, an increase in terms of angular velocity is observed for the upper block, again similarly to what was presented by Psycharis (1990). It is also possible to observe that, increasing the rotation θ_2, the postimpact velocities of the isolator and of the upper body decrease, while that of the upper body increases.

APPENDIX D

TABLE D1 List of symbols.

D	Dissipation function	$g_{sys,x}$	Linear momentum in the horizontal direction
$\mathbf{H}_{sys}(\mathbf{H}_{top})$	Angular momentum of the entire system (upper block alone)	h	Height of the center of mass of the monolithic system
I_{Gi}	Mass moment of inertia of the i-th block with respect to its centroid G	h_i	Half height of the i-th block
M	Total mass of the system	k_b	Stiffness of the isolator
$\mathbf{M}_E(\mathbf{M}_I)$	External (internal) moment vector	m	Total mass of the blocks
$\mathbf{P}_{T_i}$	Position vector transformation matrix of the i-th block	m_b	Mass of the isolator
$R(R_2)$	Size parameter for the monolithic system (upper block alone)	m_i	Mass of the i-th block
R_T	Period ratio T_p/T_b	$p(p_2)$	Frequency parameter for the monolithic system (upper block alone)
R_α	Slenderness ratio α_2/α	$\mathbf{p}_{P,R}$	Position vector of the generic point P with respect to the center of rotation R
$\mathbf{S}_{T_i}$	Displacement vector transformation matrix of the i-th block	p_s	Frequency parameter of the slenderest configuration
T	Kinetic energy	$\mathbf{s}_P$	Displacement vector of the generic point P
T_b	Period of the isolator	u_b	Horizontal displacement of the isolator
T_p	Period of the pulse	$\mathbf{v}_P$	Velocity vector of the generic point P
V	Potential energy	$\ddot{x}_g(\ddot{y}_g)$	Horizontal (vertical) component of the seismic ground acceleration
δW_{nc}	Virtual work of nonconservative forces	$\ddot{x}_{j,k}$	Threshold acceleration for the transition from pattern j to pattern k
$\mathbf{a}_E$	External acceleration vector	$\alpha(\alpha_2)$	Slenderness for the monolithic system (upper block alone)
$\mathbf{a}_{G_i,n}(\mathbf{a}_{G_i,t})$	Normal (tangential) acceleration vector of the i-th center of mass	α_s	Slenderness of the slenderest configuration
a_p	Amplitude of the pulse	γ_b	Mass ratio m/M
a_{peak}	Maximum acceleration of the LMDS oscillator	θ_i	Rotation of the i-th block
b_i	Half thickness of the i-th block	$\dot{\boldsymbol{\theta}}_i(\ddot{\boldsymbol{\theta}}_i)$	Angular velocity (acceleration) vector of the i-th block
c_b	Viscous damping of the isolator	ξ_b	Damping ratio of the isolator
$\mathbf{d}_{P,Q}$	Coordinates vector of the generic point P with respect to the center of rotation Q	ω_p	Circular frequency of the pulse
g	Gravitational acceleration		